DOE/ID/12079-87

MAGNETOTELLURIC RESPONSES OF THREE-DIMENSIONAL BODIES IN LAYERED EARTHS

by

Phillip E. Wannamaker, Stanley H. Ward and Gerald W. Hohmann

Work performed under Contract No.

DE-AC07-80ID12079

Department of Geology and Geophysics

University of Utah

Salt Lake City, Utah (USA)

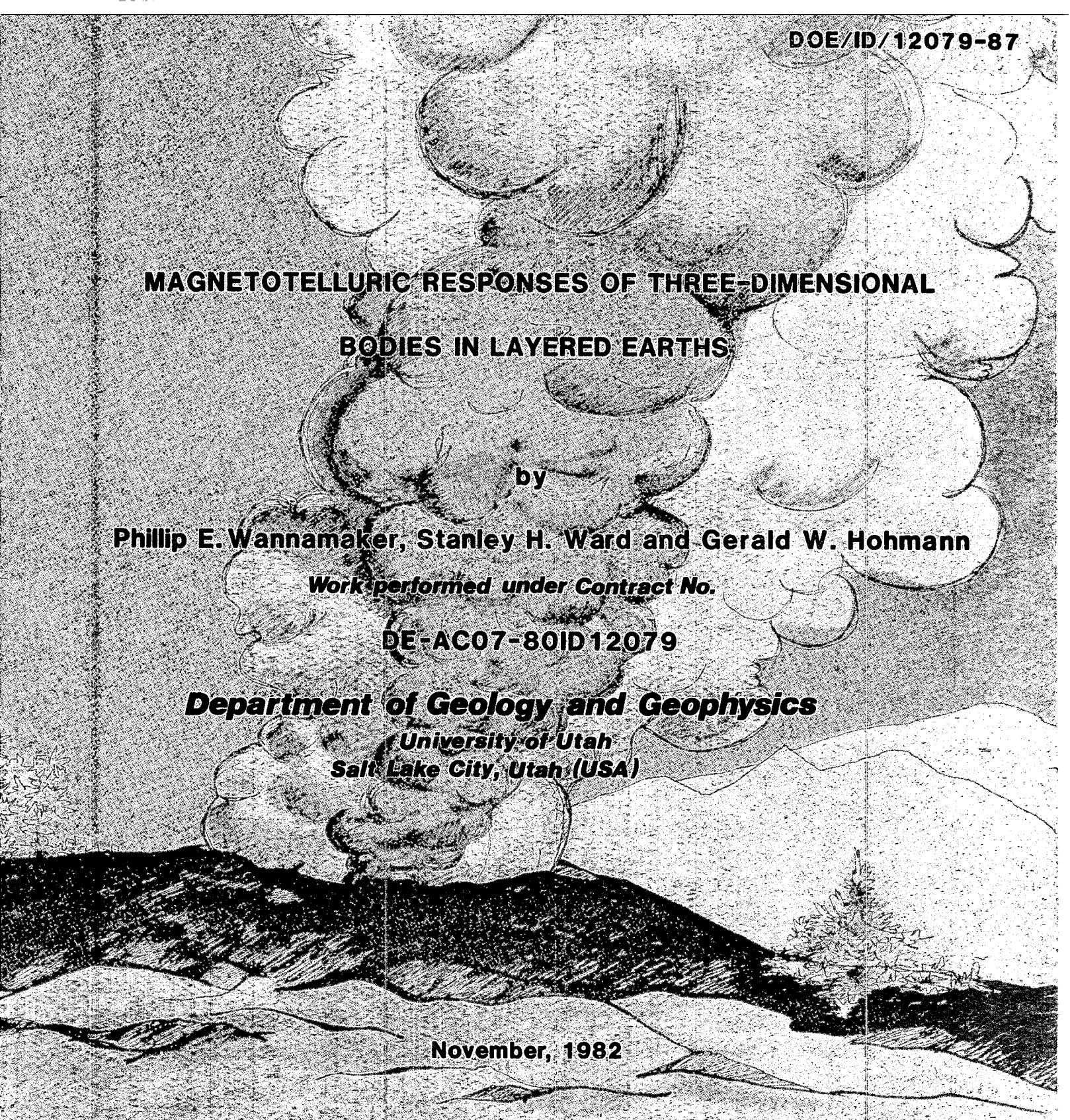

November, 1982

Prepared for

DEPARTMENT OF ENERGY

Division of Geothermal Energy

DISCLAIMER

DOE/ID/12079-87

Magnetotelluric Responses of Three-Dimensional Bodies In Layered Earths

by

P.E. Wannamaker, S.H. Ward, and G.W. Hohmann

November 1982

Department of Geology and Geophysics
University of Utah, Salt Lake City

NOTICE

This report was prepared to document work sponsored by the United States Government. Neither the United States nor its agent, the United States Department of Energy, nor any Federal employees, nor any of their contractors, subcontractors or their employees, makes any warranty, express or implied, or assumes any legal liability or responsibility for the accuracy, completeness, or usefulness of any information, apparatus, product or process disclosed, or represents that its use would not infringe privately owned rights.

NOTICE

Reference to a company or product name does not imply approval or recommendation of the product by the University of Utah or the U.S. Department of Energy to the exclusion of others that may be suitable.

TABLE OF CONTENTS

FIGURES

ABSTRACT

The electric and magnetic fields scattered by a three-dimensional inhomogeneity in a conducting earth result largely from current-gathering, a boundary polarization charge phenomenon that becomes increasingly important as frequency falls. Boundary charges cause normalized electric field magnitudes, and thus tensor apparent resistivities and magnitudes of vertical admittance elements, to remain anomalous as frequency approaches zero. However, these $\vec{E}$-field distortions below certain frequencies are essentially in-phase with the incident electric field. In addition, secondary magnetic field amplitudes over a body ultimately decline in proportion to the layered host impedance. It follows that tipper element magnitudes and all MT function phases become minimally affected at low frequencies by an inhomogeneity.

Resistivity structure in nature is a collection of inhomogeneities of various scales, and the small structures in this collection can have MT responses as strong as those of the large structures. Hence, a severe distortion due to current-gathering in any nearby, small-scale geological noise can be superimposed to arbitrarily low frequencies upon the apparent resistivities and vertical admittance magnitudes of buried targets. On the other hand, the MT responses of small and large bodies have frequency dependencies that are, in general, separated as the square of the geometric scale factor distinguishing the different bodies.

Therefore, tipper element magnitudes as well as the phases of all MT functions due to small-scale geological noise will be limited to high frequencies, so that one may "see through" geological noise with these functions to target responses occuring at lower frequencies.

The applicability of 2-D transverse electric (TE) modeling algorithms is very limited, since this 2-D mode involves no boundary charges and hence no current-gathering. Furthermore, 3-D bodies in layered hosts typical in nature, with layer resistivities that increase with depth in the upper 10 or more km, are even less amenable to 2-D TE interpretation than are similar 3-D bodies in uniform half-spaces. However, centrally located profiles across elongate 3-D prisms may be modeled accurately with a 2-D transverse magnetic (TM) algorithm, which implicitly includes current-gathering in its formulation. In defining apparent resistivity and impedance phase for TM modeling of such bodies, we recommend a coordinate system derived using tipper-strike, calculated at the frequency for which tipper magnitude due to the structure of interest is large relative to that due to any nearby geological noise.

INTRODUCTION

Magnetotelluric (MT) measurements are sensitive to the resistivity structure of the earth, potentially to depths exceeding 100 km (Cagniard, 1953; Swift, 1967; Word et al., 1971; Vozoff, 1972; Jupp and Vozoff, 1976; Larsen, 1975, 1981). Recent advances in instrumentation and data processing (e.g. Gamble et al., 1979; Weinstock and Overton, 1981; Stodt, 1982) have enabled procurement of very accurate tensor MT data. However, the skills necessary to translate these measurements into trustworthy models of subsurface resistivity have been slow in developing.

MT data are, strictly speaking, responses from three-dimensional (3-D) resistivity structure in the earth, but traditionally have been interpreted using 1-D and sometimes 2-D model structures (for example, Petrick et al., 1977; Stanley et al., 1977; Rooney and Hutton, 1977; Parker and Whaler, 1981). There are two reasons for this. First, 3-D modeling routines require considerable computing resources to handle complex earth structure, resources not readily available. The second reason, related to the first, is the lack of concensus on the interpretive errors which occur when 1-D and 2-D computational aids are used in 3-D areas.

We favor keeping the interpretation of observations as simple as possible. This philosophy underlies the major purposes of this paper,

which are as follows: first, develop magnetotelluric theory for 3-D bodies in layered earths to establish the fundamental controls on observed responses; and second, investigate the utility of 1-D and 2-D algorithms for interpreting 3-D geology. This latter goal is achievable only through rigorous, three-dimensional model studies, which we perform using the computer program of Wannamaker and Hohmann (1982).

MAGNETOTELLURIC THEORY FOR THREE-DIMENSIONAL BODIES IN LAYERED EARTHS

It is our intent here to outline the essentials that determine the magnetotelluric (MT) signatures of arbitrary 3-D bodies. The first two subsections on electromagnetic (EM) field relations and tensor MT quantities focus upon single 3-D inhomogeneities in layered earths, with special attention paid to low-frequency limits of MT responses. These are followed by an application of basic EM scaling concepts to measured MT functions, in order to distinguish the anomaly of a large structure, which may represent an exploration target, from that of a small one, which may constitute geological noise. Magnetotelluric observations in nature, of course, result from coupled inhomogeneities, and we address this matter in the final theoretical subsection with an accurate approximation to multiple body responses.

Electromagnetic Field Relations

A three-dimensional body in the earth is a source of scattered electric and magnetic fields. Establishing relations between the incident plane wave fields and the scattered and total fields, as well as exploring the behavior of these relations as frequency varies, is a step toward resolving the roles of the inhomogeneity and the host layering in creating anomalous MT quantities.

Governing Equations. - A 3-D body in an n-layered earth is shown in

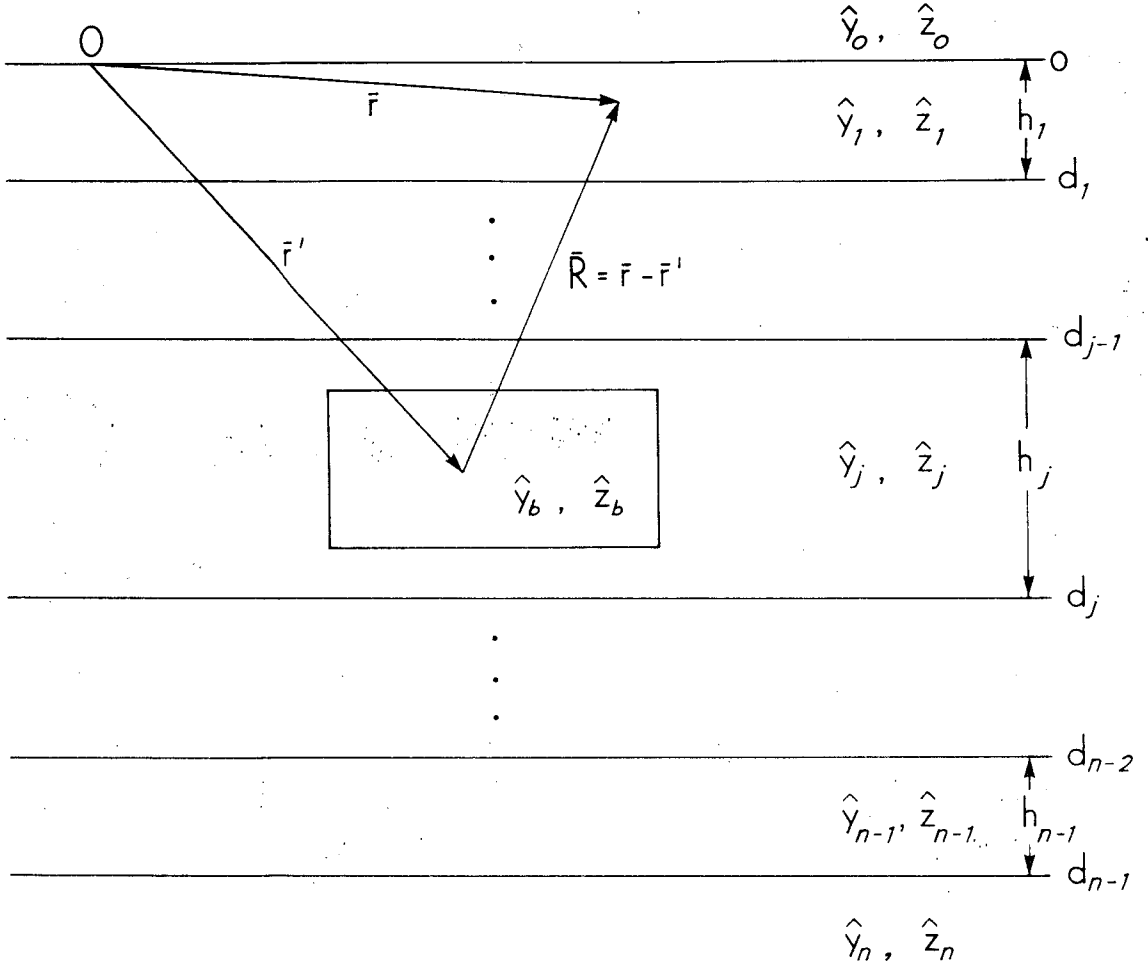

Figure 1. Section view showing physical properties of a 3-D body in a layered earth.

Figure 1. For plane wave excitation and an $e^{i\omega t}$ time dependence, Maxwell's equations,

$$-\bar{\nabla}\times\vec{E}_t = \hat{z}\vec{H}_t \tag{1}$$

and

$$\bar{\nabla}\times\vec{H}_t = \vec{J}_t \quad , \tag{2}$$

define the total electric and magnetic fields ($\vec{E}_t$, $\vec{H}_t$) as a function of position $\bar{r}$, where $\vec{J}_t = \hat{y}\vec{E}_t$ is the total current density, $\hat{y} = \sigma + i\omega\varepsilon$ is the admittivity and $\hat{z} = i\omega\mu_o$ is the impedivity. Conductivity is denoted σ, the dielectric permittivity ε is assumed constant throughout the earth and the free space value μ_o is assigned to the magnetic permeability everywhere.

Following Wannamaker and Hohmann (1982), ($\vec{E}_t$, $\vec{H}_t$) are decomposed into an incident set ($\vec{E}_i$, $\vec{H}_i$) which are the plane wave fields, and a scattered set ($\vec{E}_s$, $\vec{H}_s$), contributed by the inhomogeneity. Helmholtz equations in layer l with the body in layer j can be written

$$(\bar{\nabla}^2 + k_l^2)\vec{E}_i = 0 \quad , \tag{3}$$

$$(\bar{\nabla}^2 + k_l^2)\vec{H}_i = 0 \quad , \tag{4}$$

$$(\bar{\nabla}^2 + k_l^2)\vec{E}_s = 0 \qquad l \neq j \quad , \tag{5}$$

$$(\bar{\nabla}^2 + k_l^2)\vec{H}_s = 0 \qquad l \neq j \quad , \tag{6}$$

$$(\bar{\nabla}^2 + k_j^2)\vec{E}_s = \left(\frac{-1}{\hat{y}_j}\bar{\nabla}\bar{\nabla}\cdot + \hat{z}\right)\vec{J}_s \qquad l = j \tag{7}$$

and

$$(\bar{\nabla}^2 + k_j^2)\vec{H}_s = -\bar{\nabla} \times \vec{J}_s \qquad \ell = j \quad , \quad (8)$$

in which $k_\ell = \sqrt{-\hat{z}\hat{y}_\ell}$ is the wavenumber in layer ℓ. If the body cuts across layer interfaces, subscript j refers to any layer containing a portion of the body.

In (7) and (8), $\vec{J}_s = (\hat{y}_b - \hat{y}_j)\vec{E}_b$ is an equivalent scattering current substituting for the inhomogeneity, where $\hat{y}_b$ and $\vec{E}_b$ are the admittivity and the total electric field within the inhomogeneity. A Helmholtz equation governing $\vec{E}_b$ can be written by summing (3) and (7), provided one realizes that $\vec{E}_t = \vec{E}_b$ and that $\ell = j$ in (3). However, if one assumes for simplicity that $\hat{y}_b$ is constant within the body, then the sum of (3) and (7) can be rearranged to yield an alternate governing equation for $\vec{E}_b$, which is

$$(\bar{\nabla}^2 + k_b^2)\vec{E}_b = 0 \quad , \quad (9)$$

where $k_b = \sqrt{-\hat{z}\hat{y}_b}$.

In (7), $\frac{-1}{\hat{y}_j}\bar{\nabla}\cdot\vec{J}_s$ describes a distribution of free charge ρ on the boundary of the body. This boundary charge preserves continuity of normal $\vec{J}_t$, but in doing so makes normal $\vec{E}_t$ discontinuous across the boundary of the body, i.e.,

$$\frac{-1}{\hat{y}_j}\bar{\nabla}\cdot\vec{J}_s = \frac{\rho}{\epsilon} = \bar{\nabla}\cdot\vec{E}_t \quad . \quad (10)$$

Furthermore since $\vec{E}_i$ is continuous, $\bar{\nabla}\cdot\vec{E}_s = \bar{\nabla}\cdot\vec{E}_t$. From a physical standpoint, the charge density of (10) results from a minute, time-harmonic divergence of conduction current $\vec{J}_c = \sigma\vec{E}_t$ (Price, 1973).

The solutions for $\vec{E}_t$ and $\vec{H}_t$ in (3) through (8) are given by the

integral equations

$$\vec{E}_t(\bar{r}) = \vec{E}_i(\bar{r}) + \vec{E}_s(\bar{r}) = \vec{E}_i(\bar{r}) + \int_v (\hat{y}_b - \hat{y}_j)\, \tilde{\tilde{G}}_l^E(\bar{r};\bar{r}') \cdot \vec{E}_b(\bar{r}')\, dv' \qquad (11)$$

and

$$\vec{H}_t(\bar{r}) = \vec{H}_i(\bar{r}) + \vec{H}_s(\bar{r}) = \vec{H}_i(\bar{r}) + \int_v (\hat{y}_b - \hat{y}_j)\, \tilde{\tilde{G}}_l^H(\bar{r};\bar{r}') \cdot \vec{E}_b(\bar{r}')\, dv' \quad , \qquad (12)$$

which are also valid within the body. The 3 x 3 dyadic Green's functions $\tilde{\tilde{G}}_l^E(\bar{r};\bar{r}')$ and $\tilde{\tilde{G}}_l^H(\bar{r};\bar{r}')$ relate a vector field at $\bar{r}$ in layer l to a current element at $\bar{r}'$ in layer j including $l = j$ (Wannamaker and Hohmann, 1982).

Tensor Field Relations. - Considering the linearity of all previous equations, we postulate

$$\vec{E}_t^{\,o}(\bar{r}) = \vec{E}_i^{\,o} + \tilde{\tilde{P}}_s^{\,o}(\bar{r}) \cdot \vec{E}_i^{\,o} \qquad (13)$$

and

$$\vec{H}_t^{\,o}(\bar{r}) = \vec{H}_i^{\,o} + \tilde{\tilde{Q}}_s^{\,o}(\bar{r}) \cdot \vec{E}_i^{\,o} \quad , \qquad (14)$$

where superscript ^{o} indicates $\bar{r}$ is at the surface of the earth over which $\vec{E}_i^{\,o}$ is constant. $\tilde{\tilde{P}}_s^{\,o}(\bar{r})$ and $\tilde{\tilde{Q}}_s^{\,o}(\bar{r})$ are 3 x 2 normalized tensors representing the scattered fields unique for a specified 3-D body, layered host and frequency, of the form

$$\tilde{\tilde{P}}_s^{\,o}(\bar{r}) = \begin{bmatrix} \tilde{\tilde{P}}_h^{\,o}(\bar{r}) \\ \hline \tilde{P}_v^{\,o}(\bar{r}) \end{bmatrix} = \begin{bmatrix} P_{xx}^o & P_{xy}^o \\ P_{yx}^o & P_{yy}^o \\ \hline P_{zx}^o & P_{zy}^o \end{bmatrix} \qquad (15)$$

and

$$\tilde{Q}_s^o(\bar{r}) = \begin{bmatrix} \tilde{Q}_h^o(\bar{r}) \\ \hline \tilde{Q}_v^o(\bar{r}) \end{bmatrix} = \left[\begin{array}{cc} Q_{xx}^o & Q_{xy}^o \\ Q_{yx}^o & Q_{yy}^o \\ \hline Q_{zx}^o & Q_{zy}^o \end{array}\right] \tag{16}$$

Note that we have subdivided the scattered field tensors into horizontal subtensors, $\tilde{P}_h^o(\bar{r})$ and $\tilde{Q}_h^o(\bar{r})$, and vertical subtensors, $\tilde{P}_v^o(\bar{r})$ and $\tilde{Q}_v^o(\bar{r})$, which pertain respectively to horizontal and vertical electric and magnetic field components induced by the incident electric vector $\vec{E}_i^o$. Discrete, approximate versions of $\tilde{P}_s^o(\bar{r})$ and $\tilde{Q}_s^o(\bar{r})$ are computed by Wannamaker and Hohmann (1982), and Larsen (1975, 1977, 1981) and Klein and Larsen (1978) have also considered $\vec{E}$- and $\vec{H}$-field tensor approaches.

The incident fields at the surface are related through

$$\vec{E}_i^o = \tilde{Z}_\ell \cdot \vec{H}_i^o \tag{17}$$

(Cagniard, 1953; Ward, 1967, p. 117-124), with the layered earth impedance

$$\tilde{Z}_\ell = \begin{bmatrix} 0 & Z_\ell \\ -Z_\ell & 0 \end{bmatrix} \tag{18}$$

In equations (13) and (14), $\vec{E}_t^o(\bar{r})$ and $\vec{H}_t^o(\bar{r})$ referred to total electric and magnetic fields at the earth's surface, including vertical field components. Subsequently, however, $\vec{E}_t^o(\bar{r})$ and $\vec{H}_t^o(\bar{r})$ will denote just the horizontal total fields at the surface, since we will need these fields to define magnetotelluric tensor quantities. Using (13) through (17), and with $\tilde{I}$ the 2 x 2 identity tensor, the horizontal fields become

$$\vec{E}_t^{\,o}(\bar{r}) = \left[\tilde{I} + \tilde{P}_h^{\,o}(\bar{r})\right]\cdot\vec{E}_i^{\,o} \tag{19}$$

and

$$\vec{H}_t^{\,o}(\bar{r}) = \left[\tilde{I} + \tilde{Q}_h^{\,o}(\bar{r})\cdot\tilde{Z}_\ell\right]\cdot\vec{H}_i^{\,o} \quad . \tag{20}$$

Low Frequency Conditions. - At low frequencies, such that $|k_\ell \bar{R}| \ll 1$ for all ℓ, where $\bar{R} = \bar{r} - \bar{r}'$ in Figure 1 is the observation distance from the body, the Helmholtz equations (3) through (8) become

$$\bar{\nabla}^2\vec{E}_i \simeq 0 \quad , \tag{21}$$

$$\bar{\nabla}^2\vec{H}_i \simeq 0 \quad , \tag{22}$$

$$\bar{\nabla}^2\vec{E}_s \simeq 0 \qquad \ell \neq j \quad , \tag{23}$$

$$\bar{\nabla}^2\vec{H}_s \simeq 0 \qquad \ell \neq j \quad , \tag{24}$$

$$\bar{\nabla}^2\vec{E}_s \simeq \frac{-1}{\hat{\gamma}_j}\bar{\nabla}\bar{\nabla}\cdot\vec{J}_s = \frac{1}{\epsilon}\bar{\nabla}\rho \qquad \ell = j \tag{25}$$

and

$$\bar{\nabla}^2\vec{H}_s \simeq -\bar{\nabla}\times\vec{J}_s \qquad \ell = j \quad , \tag{26}$$

which are Laplace's and Poisson's equations. In particular, note that the volume current source term $\hat{z}\vec{J}_s$ in equation (7) is not present in equation (25). This term, to first order, is proportional to ω so that, from equations (10) and (25), $\vec{E}_s^{\,o}(\bar{r})$ and thus $\tilde{P}_s^{\,o}(\bar{r})$ at low frequencies are determined solely by the boundary charge ρ.

This is not to say that it is necessarily valid to treat the secondary fields given by (23) through (26) as though they were induced by a zero-frequency incident electric field. Equations (9), (10), and

(25) together show that the charge density ρ is intimately associated with the $\vec{E}$-field inside the inhomogeneity. Also, the $\vec{E}$-field interior to the body defines $\vec{J}_s$, which in turn provides the source for the secondary magnetic field in (26). For very conductive inhomogeneities over a certain range of frequencies, Laplace's equation may be a poor representation of the electric field behavior within the body, even though Laplace's and Poisson's equations could be accurate exterior to the body in the more resistive host. We thus require frequencies sufficiently low so that wavelengths within the inhomogeneity are long compared to the size of the inhomogeneity before assuming that (9) reduces to

$$\tilde{\nabla}^2 \vec{E}_b \simeq 0 \qquad (27)$$

This interior long-wavelength criterion may be written symbolically as $|k_b L| << 1$, where L is some characteristic dimension of the body. The dimension L of course differs from body to body; to quantify it rigorously requires computer simulation of the electromagnetic response of the particular body under consideration. Quantifying low-frequency MT reponses over resistivity structures of interest to the geophysical community receives major emphasis in the model studies performed in this paper. Nevertheless, our low-frequency analysis provides the following fundamental concept: when both long-wavelength criteria, $|k_z \bar{R}| << 1$ and $|k_b L| << 1$, are satisfied, then $\tilde{P}_s^o(\bar{r})$ and $\tilde{Q}_s^o(\bar{r})$ will be essentially real and independent of frequency. Thus, the layered host plus the inhomogeneity define the frequency dependence of electromagnetic measurements.

Perhaps the most important conclusion to reach from the development

to this point is that boundary polarization charges, acting through equation (25), cause $\vec{E}_t^o(\bar{r})$ near a 3-D body to remain anomalous to arbitrarily low frequencies. Such anomalous behavior due to ρ, when it occurs about conductive bodies, is referred to as current-gathering by various investigators (e.g., Berdichevskiy and Dmitriev, 1976).

Current-gathering, however, leads to no such effect on $\vec{H}_t^o(\bar{r})$ as frequency falls. Over an arbitrarily layered earth, it is not difficult to show that $|Z_\ell|$ decreases monotonically with decreasing frequency (see Cagniard, 1953). In particular, for a uniform half-space, we have

$$|Z_\ell| = \left|\frac{\omega\mu_o}{k_1}\right| \simeq \sqrt{\frac{\omega\mu_o}{\sigma_1}} \quad , \tag{28}$$

indicating that $\tilde{Z}_\ell$ varies as $\omega^{1/2}$. Hence, even though $\tilde{Q}_s^o(\bar{r})$ possesses a non-zero, low-frequency limit, $\vec{H}_s^o(\bar{r}) = \tilde{Q}_s^o(\bar{r})\cdot\tilde{Z}_\ell\cdot\vec{H}_i^o$ will vanish as frequency approaches zero.

Tensor Magnetotelluric Quantities

The tensor field relations we have specified may be used to construct MT functions. In doing so, the relative contributions of the body and the layered host to anomalous MT functions become evident. Studies of MT functions over single bodies, and in particular the low-frequency asymptotes of such quantities, are required before such functions over multiple bodies can be understood.

Impedance Tensor. - The existence of the general impedance tensor $\tilde{Z}(\bar{r})$, defined by

$$\vec{E}_t^o(\bar{r}) = \tilde{Z}(\bar{r})\cdot\vec{H}_t^o(\bar{r}) \quad , \tag{29}$$

where $\tilde{Z}(\bar{r})$ is of the form

$$\tilde{\tilde{Z}}(\bar{r}) = \begin{bmatrix} Z_{xx} & Z_{xy} \\ Z_{yx} & Z_{yy} \end{bmatrix} , \tag{30}$$

can be demonstrated by substituting (19) and (20) into (17). One obtains

$$\tilde{\tilde{Z}}(\bar{r}) = [\tilde{\tilde{I}} + \tilde{\tilde{P}}_h^o(\bar{r})]\cdot\tilde{\tilde{Z}}_\ell\cdot[\tilde{\tilde{I}} + \tilde{\tilde{Q}}_h^o(\bar{r})\cdot\tilde{\tilde{Z}}_\ell]^{-1} . \tag{31}$$

Whenever observation points are on, and measurement axes are parallel to axes of symmetry of a 3-D body, $\tilde{\tilde{P}}_h^o(\bar{r})$ is diagonal and $\tilde{\tilde{Q}}_h^o(\bar{r})$ and $\tilde{\tilde{Z}}(\bar{r})$ are antidiagonal.

As frequency approaches zero, so that $|k_z\bar{R}|$, $|k_b L|$ and $|Z_\ell Q_{ij}^o|$ $<< 1$, equation (31) reduces to

$$\tilde{\tilde{Z}}(\bar{r}) \simeq [\tilde{\tilde{I}} + \tilde{\tilde{P}}_h^o(\bar{r})]\cdot\tilde{\tilde{Z}}_\ell . \tag{32}$$

All four elements Z_{ij} of $\tilde{\tilde{Z}}(\bar{r})$ are related to Z_ℓ by real constants, so that in this low-frequency limit a Hilbert Transform relates magnitude and phase of Z_{ij} (Kunetz, 1972; Boehl et al., 1977).

The apparent resistivities at low frequencies are, from (32),

$$\rho_{xx} \simeq \frac{1}{\omega\mu_o}|Z_\ell|^2\cdot|P_{xy}^o|^2 , \tag{33a}$$

$$\rho_{xy} \simeq \frac{1}{\omega\mu_o}|Z_\ell|^2\cdot|1 + P_{xx}^o|^2 , \tag{33b}$$

$$\rho_{yx} \simeq \frac{1}{\omega\mu_o}|Z_\ell|^2\cdot|1 + P_{yy}^o|^2 \tag{33c}$$

and

$$\rho_{yy} \simeq \frac{1}{\omega\mu_o}|Z_\ell|^2\cdot|P_{yx}^o|^2 \tag{33d}$$

for a 3-D body. Like Z_{ij}, all ρ_{ij} are distorted to arbitrarily low frequencies by boundary charge effects and are related to $\rho_\ell = \frac{1}{\omega\mu_0}|Z_\ell|^2$ by positive constants as given in (33). If interpreted assuming a 1-D model structure, apparent resistivity soundings distorted in this manner by a nearby 3-D body will yield model resistivities in error by a factor ρ_{ij}/ρ_ℓ and model layer thickness in error by $\sqrt{\rho_{ij}/\rho_\ell}$ (Larsen, 1977, 1981).

However, since P^o_{ij} become real as frequency approaches zero, the phases of all Z_{ij} (i.e., ϕ_{ij}) asymptote to the phase of the layered host impedance ϕ_ℓ and are no longer affected by the inhomogeneity. Nevertheless, this does not mean that the parameters of the layered host can be recovered through one-dimensional inversion of the impedance phase sounding alone. It is well known in the literature (for example, Cagniard, 1953), and can be inferred from equations (32) and (33), that a specific impedance phase sounding can correspond to an infinite number of apparent resistivity soundings, and thus an infinite number of layered resistivity structures.

Let us now briefly consider a two-dimensional inhomogeneity, whose strike direction corresponds to the x coordinate axis. An x-oriented incident electric field induces only x-oriented secondary $\vec{E}$-fields about such a structure, so that the total electric field parallels all resistivity contacts and no boundary charges exist. This is the transverse electric (TE) mode of wave polarization (Swift, 1967). At low frequencies for the TE mode, neither volume currents nor boundary charges contribute as sources for a secondary electric field; therefore, P^o_{xx} becomes zero and ρ_{xy} in (33b) approaches ρ_ℓ. Similarly,

a y-oriented incident electric field causes only y-oriented secondary $\vec{E}$-fields over a 2-D body. Such a field polarization defines the transverse magnetic (TM) mode. However, since the incident electric field for this mode is normal to resistivity contacts in the earth, boundary polarization charges will be induced as sources for secondary $\vec{E}$-fields, P^{o}_{yy} will have a non-zero value to arbitrarily low frequencies and ρ_{yx} remains defined by (33c). Because of boundary charges, the TM mode in the case of conductive bodies exhibits two-dimensional current-gathering. Thus, if all near-surface geological noise were two-dimensional, then one-dimensional inversion of apparent resistivity and impedance phase soundings identified as TE would yield models of deep resistivity layering that are relatively free from distortion due to such noises (Word et al., 1971; Vozoff, 1972; Berdichevsky and Dmitriev, 1976). In our opinion, however, geological noise in nature is generally not two-dimensional.

Vertical $\vec{H}$-Field Tensors. - Vertical magnetic field transfer functions are defined by (Word et al., 1971)

$$\vec{H}^{o}_{z}(\bar{r}) = \tilde{K}_{z}(\bar{r}) \cdot \vec{H}^{o}_{t}(\bar{r}) \tag{34}$$

and

$$\vec{H}^{o}_{z}(\bar{r}) = \tilde{Y}_{z}(\bar{r}) \cdot \vec{E}^{o}_{t}(\bar{r}) \quad , \tag{35}$$

in which

$$\tilde{K}_{z}(\bar{r}) = [K_{zx}\ K_{zy}] \tag{36}$$

and

$$\tilde{\bar{Y}}_z(\bar{r}) = [Y_{zx}\ Y_{zy}] \quad . \tag{37}$$

In terms of scattered field tensors we have

$$\tilde{\bar{K}}_z(\bar{r}) = \tilde{\bar{Q}}_v^o(\bar{r}) \cdot \tilde{\bar{Z}}_\ell \cdot [\tilde{\bar{I}} + \tilde{\bar{Q}}_h^o(\bar{r}) \cdot \tilde{\bar{Z}}_\ell]^{-1} \tag{38}$$

and

$$\tilde{\bar{Y}}_z(\bar{r}) = \tilde{\bar{Q}}_v^o(\bar{r}) \cdot [\tilde{\bar{I}} + \tilde{\bar{P}}_h^o(\bar{r})]^{-1} \tag{39}$$

The low frequency asymptotes of the tensor elements are

$$K_{zx} \simeq -Z_\ell Q_{zy}^o \quad , \tag{40a}$$

$$K_{zy} \simeq Z_\ell Q_{zx}^o \quad , \tag{40b}$$

$$Y_{zx} \simeq \left[\frac{Q_{zx}^o(1+P_{yy}^o) - Q_{zy}^o P_{yx}^o}{(1+P_{xx}^o)(1+P_{yy}^o) - P_{xy}^o P_{yx}^o} \right] \tag{41a}$$

and

$$Y_{zy} \simeq \left[\frac{Q_{zy}^o(1+P_{xx}^o) - Q_{zx}^o P_{xy}^o}{(1+P_{xx}^o)(1+P_{yy}^o) - P_{xy}^o P_{yx}^o} \right] \quad . \tag{41b}$$

Note that K_{zx} and K_{zy} are related to Z_ℓ by real constants, so their magnitudes approach zero as frequency approaches zero. In addition, phases of K_{zx} and K_{zy} approach ϕ_ℓ as frequency falls, since $\tilde{\bar{Q}}_v^o(\bar{r})$ becomes real. However, due to polarization charges, $|Y_{zx}|$ and $|Y_{zy}|$ remain permanently distorted as frequency drops, although the phases will asymptote to zero (or 180°). Even over a 2-D body, $\tilde{\bar{Y}}_z(\bar{r})$ remains anomalous as frequency drops, since in the low-frequency limit we have $Y_{zx} \simeq Q_{zx}^o$.

The tipper (Vozoff, 1972) has a magnitude given by

$$|T| = [|K_{zx}|^2 + |K_{zy}|^2]^{1/2} \quad . \quad (42)$$

From equation (40), at low frequencies, the tipper becomes

$$|T| \simeq |Z_\ell| \cdot [|Q^o_{zy}|^2 + |Q^o_{zx}|^2]^{1/2} \quad , \quad (43)$$

which approaches zero as $\omega \to 0$. Furthermore, because of $\tilde{Z}_\ell$, T and $\tilde{K}_z(\bar{r})$ contain a great deal of information about the layered host.

Analogous to tipper, one may define a vertical admittance function A, of magnitude given by

$$|A| = [|Y_{zx}|^2 + |Y_{zy}|^2]^{1/2} \quad . \quad (44)$$

Substitution of (41) into (44) shows that anomalies in A over an inhomogeneity will exist to vanishingly low frequencies, since there is no attenuation by $\tilde{Z}_\ell$ as in the case of the tipper. On the other hand, the absence of $\tilde{Z}_\ell$ in the definitions of A and $\tilde{Y}_z(\bar{r})$ means that these quantities are determined more exclusively by the inhomogeneity as opposed to the layered host than is the tipper, though there is some information about the layering in $\tilde{P}^o_s(\bar{r})$ and $\tilde{Q}^o_s(\bar{r})$ (Wannamaker and Hohmann, 1982).

Behavior of MT Quantities under EM Scaling

While our discussion to this point has been confined to single bodies, we must recognize that natural resistivity structure is an ensemble of inhomogeneities of various scales within a layered host. The following specific application of standard electromagnetic scaling concepts (Stratton, 1941, p. 488-490; Grant and West, 1965, p. 478-482) can aid in discriminating large bodies from small bodies on the basis of

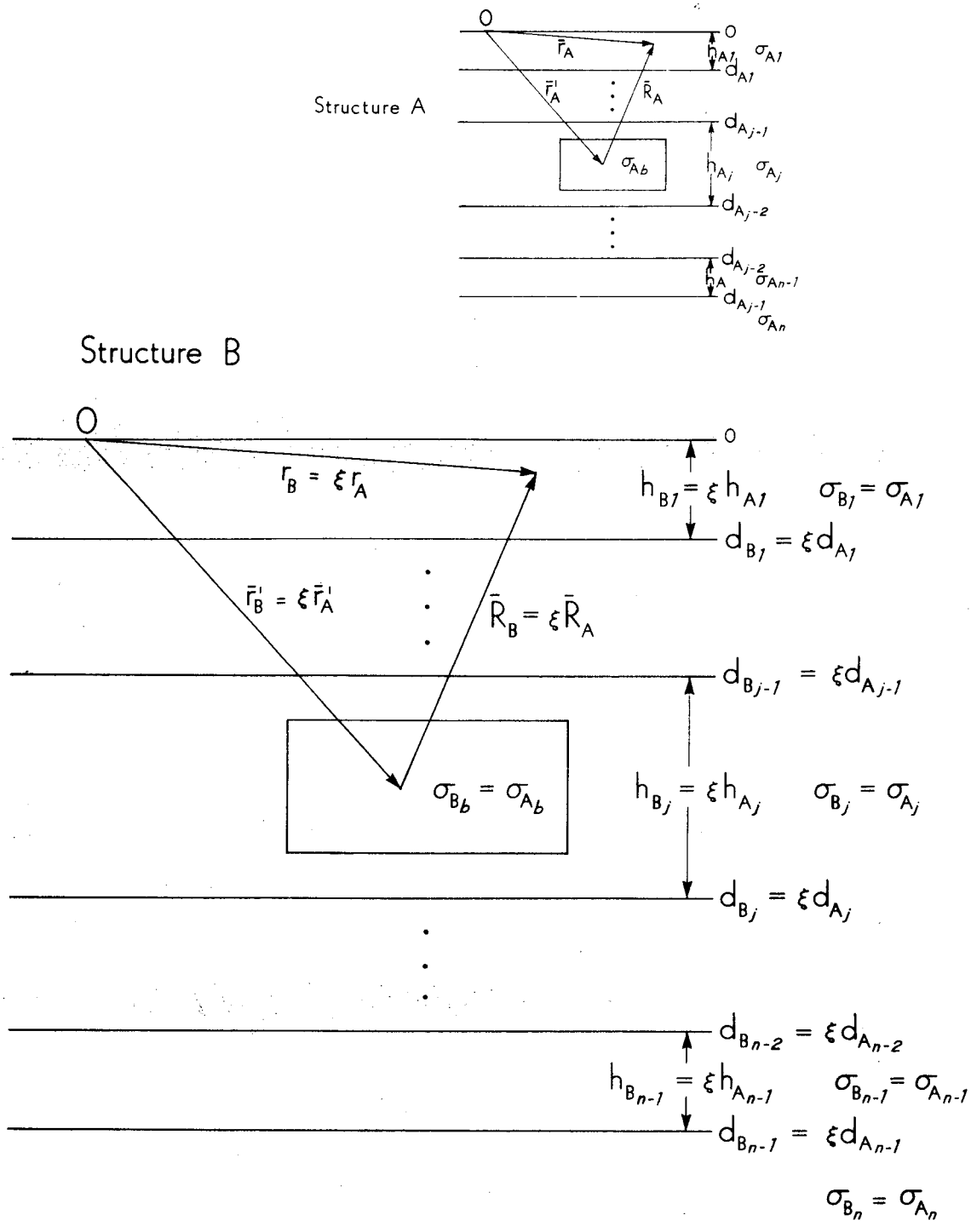

Figure 2. Scaled conductivity distributions used in discussion of EM scaling. Values of conductivity at corresponding points in body or layering have been preserved, i.e., $\sigma_A(\bar{r}_A) = \sigma_B(\bar{r}_B)$.

the frequency dependence of their MT responses.

Consider geometries A and B of Figure 2, identical except for a dimensional scaling of the second with respect to the first by a factor ξ. We define the conductivity distributions $\sigma_A(\bar{r}_A)$ and $\sigma_B(\bar{r}_B)$ of Figure 2 to include both inhomogeneity and host layering of geometries A and B, and set them equal to each other (i.e., $\sigma_B(\bar{r}_B) = \sigma_A(\bar{r}_A)$). The structures are excited by incident fields $(\vec{E}^o_{iA}, \vec{H}^o_{iA})$ and $(\vec{E}^o_{iB}, \vec{H}^o_{iB})$ of different frequencies, ω_A and $\omega_B = \frac{1}{\xi^2}\omega_A$, so that an induction number,

$$\tilde{\theta} = \omega_A \mu_o \sigma_A(\bar{r}_A)|\bar{r}_A|^2 \hat{r} = \omega_B \mu_o \sigma_B(\bar{r}_B)|\bar{r}_B|^2 \hat{r} \quad , \tag{45}$$

is preserved, where $\hat{r}$ is a unit vector in the $\bar{r}$ direction and we ignore displacement currents in the earth.

Under such scaling, secondary field tensors $\tilde{\tilde{P}}^o_s(\bar{r})$ and $\tilde{\tilde{R}}^o_s(\bar{r})$, remain invariant, where

$$\vec{H}^o_s(\bar{r}) = \tilde{\tilde{R}}^o_s(\bar{r}) \cdot \vec{H}^o_i \tag{46}$$

and

$$\tilde{\tilde{R}}^o_s(\bar{r}) = \tilde{\tilde{Q}}^o_s(\bar{r}) \cdot \tilde{\tilde{Z}}_\ell \quad , \tag{47}$$

and where $\tilde{\tilde{R}}^o_s(\bar{r})$ is of a form identical to that of $\tilde{\tilde{P}}^o_s(\bar{r})$ and $\tilde{\tilde{Q}}^o_s(\bar{r})$ in (15) and (16). In other words, similitude requires that we have

$$\tilde{\tilde{P}}^o_{sA}(\bar{r}_A) = \tilde{\tilde{P}}^o_{sB}(\bar{r}_B) = \tilde{\tilde{P}}^o_s(\tilde{\theta}) \tag{48}$$

and

$$\tilde{\tilde{R}}^o_{sA}(\bar{r}_A) = \tilde{\tilde{R}}^o_{sB}(\bar{r}_B) = \tilde{\tilde{R}}^o_s(\tilde{\theta}) \quad . \tag{49}$$

This is not so with $\tilde{\tilde{Z}}_\ell$ or $\tilde{\tilde{Q}}^o_s(\bar{r})$ individually. In fact, in terms of the structures of Figure 2, one may show from Cagniard (1953) that

$$\tilde{\tilde{Z}}_{\ell A} = \xi \tilde{\tilde{Z}}_{\ell B} \tag{50}$$

for an arbitrarily layered earth, and that hence from (47) and (49),

$$\tilde{\tilde{Q}}^o_{sA}(\bar{r}_A) = \frac{1}{\xi} \tilde{\tilde{Q}}^o_{sB}(\bar{r}_B) \tag{51}$$

However, the phase of the layered host impedance is invariant to scaling, (Cagniard, 1953), meaning

$$\phi_{\ell A} = \phi_{\ell B} = \phi_\ell(\bar{\theta}) \tag{52}$$

One may continue, using (31), (48), (50) and (51), to show that

$$\tilde{\tilde{Z}}_A(\bar{r}_A) = \xi \tilde{\tilde{Z}}_B(\bar{r}_B) \tag{53}$$

leading to

$$\rho_{ijA} = \rho_{ijB} = \rho_{ij}(\bar{\theta}) \tag{54}$$

and

$$\phi_{ijA} = \phi_{ijB} = \phi_{ij}(\bar{\theta}) \tag{55}$$

Furthermore, from equation (38), (50) and (51),

$$\tilde{\tilde{K}}_{zA}(\bar{r}_A) = \tilde{\tilde{K}}_{zB}(\bar{r}_B) = \tilde{K}_z(\bar{\theta}) \tag{56}$$

However, (39), (48) and (51) lead to the equality

$$\tilde{\tilde{Y}}_{zA}(\bar{r}_A) = \frac{1}{\xi} \tilde{\tilde{Y}}_{zB}(\bar{r}_B) \tag{57}$$

This has been a rather restricted discussion of EM scaling. In

particular, we needed to scale layer thicknesses in addition to body dimensions for the equations to be strictly valid, whereas the real earth consists of multiple inhomogeneities within a single layered sequence. A consideration of bodies in uniform half-spaces would have circumvented this difficulty, but with an attendant loss of generality. The requirement that corresponding media between structures A and B have equal conductivities is a further limitation, which is not necessary in all applications of similitude.

The specialized nature of this development, however, does not detract from the fundamental conclusion of equations (54) through (57): small inhomogeneities can have MT responses as strong as those of large ones, although the small and large body responses have frequency dependences that are, all else being equal, separated as the square of the geometric scale factor distinguishing the different bodies. An exception is the magnitude of $\tilde{Y}_z(\bar{r})$, for which large structures yield greater anomalies than do small ones, although the aforesaid separation of responses in frequency still occurs.

Coupled Body Theory

We are finally in a position to study the MT responses of coupled inhomogeneities in a layered earth. The forthcoming analysis is approximate, but calculations in Appendix A verify its accuracy. Furthermore, the framework of the development is very convenient, in that it allows straightforward application of the relations of our EM scaling study.

Consider simply two adjacent structures, A and B, for example as in

Figure A-1, the latter of a scale several times greater than the former. Fields scattered solely from the larger structure may be sufficiently constant over the smaller to behave, with the incident plane waves, as uniform total source fields for the smaller body. It is thus assumed that $\vec{J}_s$ within the larger body is affected negligibly by the smaller. In addition, for simplicity, we consider the smaller structure A to be outcropping.

Horizontal Field Relations. - Secondary horizontal fields at the surface scattered from the smaller structure A by itself, in terms of the incident electric field, are written

$$\vec{E}^{\,o}_{sA}(\bar{r}) = \tilde{P}^{o}_{hA}(\bar{r})\cdot\vec{E}^{\,o}_{i} \tag{58}$$

and

$$\vec{H}^{\,o}_{sA}(\bar{r}) = \tilde{Q}^{o}_{hA}(\bar{r})\cdot\vec{E}^{\,o}_{i} \tag{59}$$

Note that henceforth we define $\vec{E}^{\,o}_{s}(\bar{r})$ and $\vec{H}^{o}_{s}(\bar{r})$ about either structure A or structure B to contain only horizontal components. If the total horizontal fields about the larger body alone are given by

$$\vec{E}^{\,o}_{tB}(\bar{r}) = [\tilde{I} + \tilde{P}^{o}_{hB}(\bar{r})]\cdot\vec{E}^{\,o}_{i} \tag{60}$$

and

$$\vec{H}^{\,o}_{tB}(\bar{r}) = [\tilde{I} + \tilde{Q}^{o}_{hB}(\bar{r})\cdot\tilde{Z}_{\ell}]\cdot\vec{H}^{\,o}_{i} \quad , \tag{61}$$

then perturbed horizontal secondary fields scattered by the smaller body located at $\bar{r}_A$ are

$$\vec{E}^{\,o\prime}_{sA}(\bar{r}) \simeq \tilde{P}^{o}_{hA}(\bar{r})\cdot[\tilde{I} + \tilde{P}^{o}_{hB}(\bar{r}_A)]\cdot\vec{E}^{\,o}_{i} \tag{62}$$

and

$$\vec{H}^{o\prime}_{sA}(\bar{r}) \simeq \tilde{Q}^{o}_{hA}(\bar{r}) \cdot [\tilde{I} + \tilde{P}^{o}_{hB}(\bar{r}_A)] \cdot \vec{E}^{o}_{i} \qquad (63)$$

An approximate impedance defined by

$$[\vec{E}^{o}_{tB}(\bar{r}) + \vec{E}^{o\prime}_{sA}(\bar{r})] \simeq \tilde{\tilde{Z}}(\bar{r}) \cdot [\vec{H}^{o}_{tB}(\bar{r}) + \vec{H}^{o\prime}_{sA}(\bar{r})] \qquad (64)$$

results from (60) through (63), giving

$$\begin{aligned} \tilde{\tilde{Z}}(\bar{r}) \simeq & \{\tilde{I} + \tilde{P}^{o}_{hB}(\bar{r}) + \tilde{P}^{o}_{hA}(\bar{r}) \cdot [\tilde{I} + \tilde{P}^{o}_{hB}(\bar{r}_A)]\} \cdot \tilde{\tilde{Z}}_{\ell} \\ & \cdot \{\tilde{I} + \tilde{Q}^{o}_{hB}(\bar{r}) \cdot \tilde{\tilde{Z}}_{\ell} + \tilde{Q}^{o}_{hA}(\bar{r}) \cdot [\tilde{I} + \tilde{P}^{o}_{hB}(\bar{r}_A)] \cdot \tilde{\tilde{Z}}_{\ell}\}^{-1} \end{aligned} \qquad (65)$$

This expression for the coupled body impedance quantifies the distortion of the apparent resistivity signature of a large inhomogeneity, perhaps representing a buried target, resulting from current-gathering in a small-scale near-surface inhomogeneity, which may constitute geological noise. The key is equation (48) of the previous EM scaling discussion which indicates that $\tilde{P}^{o}_{hA}(\bar{r})$ may be as great as $\tilde{P}^{o}_{hB}(\bar{r})$ near the smaller structure, even at low frequencies. However, only a minor effect on the impedance by the magnetic field of the smaller structure is likely at all but high frequencies when the larger body is not responding, since equation (51) holds that $\tilde{Q}^{o}_{hB}(\bar{r})$ is generally much greater than $\tilde{Q}^{o}_{hA}(\bar{r})$.

The impedance phase response of the larger body may suffer some effect due to the smaller body, even at low frequencies where $\tilde{P}^{o}_{hA}(\bar{r})$ is essentially real. This is chiefly because $\tilde{P}^{o}_{hB}(\bar{r}_A)$ is not a diagonal tensor, as can be verified by assuming $\tilde{P}^{o}_{hB}(\bar{r}_A) \simeq \tilde{P}^{o}_{hB}(\bar{r})$ in the vicinity of structure A and expanding $\tilde{\tilde{Z}}(\bar{r})$ of (65) into its individual elements

Z_{ij}. If coordinate axes can be chosen such that $\tilde{P}_{hB}(\bar{r}_A)$ is nearly diagonal, this problem should be inconsequential, and methods of ascertaining these axes in the presence of small-scale geological noise will be developed in upcoming sections of this paper.

Vertical Magnetic Field Relations. - A similar analysis is possible for $\tilde{K}_z(\bar{r})$ and $\tilde{Y}_z(\bar{r})$. Letting the vertical magnetic field over the smaller structure alone be given by

$$\vec{H}^{\circ}_{zA}(\bar{r}) = \tilde{Q}^{\circ}_{vA}(\bar{r}) \cdot \vec{E}^{\circ}_{i} \quad , \tag{66}$$

then the perturbed vertical field in the presence of structure B is

$$\vec{H}^{\circ\prime}_{zA}(\bar{r}) \simeq \tilde{Q}^{\circ}_{vA}(\bar{r}) \cdot [\tilde{I} + \tilde{P}^{\circ}_{hB}(\bar{r}_A)] \cdot \vec{E}^{\circ}_{i} \quad . \tag{67}$$

The vertical field of the larger structure B is

$$\vec{H}^{\circ}_{zB}(\bar{r}) = \tilde{Q}^{\circ}_{vB}(\bar{r}) \cdot \vec{E}^{\circ}_{i} \quad . \tag{68}$$

We now introduce the approximate definitions

$$[\vec{H}^{\circ}_{zB}(\bar{r}) + \vec{H}^{\circ\prime}_{zA}(\bar{r})] \simeq \tilde{K}_z(\bar{r}) \cdot [\vec{H}^{\circ}_{tB}(\bar{r}) + \vec{H}^{\circ\prime}_{sA}(\bar{r})] \tag{69}$$

and

$$[\vec{H}^{\circ}_{zB}(\bar{r}) + \vec{H}^{\circ\prime}_{zA}(\bar{r})] \simeq \tilde{Y}_z(\bar{r}) \cdot [\vec{E}^{\circ}_{tB}(\bar{r}) + \vec{E}^{\circ\prime}_{sA}(\bar{r})] \quad . \tag{70}$$

With equations (60) through (63), (67) and (68), the vertical field transfer tensors of (69) and (70) are

$$\begin{aligned} \tilde{K}_z(\bar{r}) \simeq & \left\{ \tilde{Q}^{\circ}_{vB}(\bar{r}) + \tilde{Q}^{\circ}_{vA}(\bar{r}) \cdot [\tilde{I} + \tilde{P}^{\circ}_{hB}(\bar{r}_A)] \right\} \cdot \tilde{Z}_{\ell} \\ & \cdot \left\{ \tilde{I} + \tilde{Q}^{\circ}_{hB}(\bar{r}) \cdot \tilde{Z}_{\ell} + \tilde{Q}^{\circ}_{hA}(\bar{r}) \cdot [\tilde{I} + \tilde{P}^{\circ}_{hB}(\bar{r}_A)] \cdot \tilde{Z}_{\ell} \right\}^{-1} \end{aligned} \tag{71}$$

and

$$\tilde{Y}_z(\bar{r}) \simeq \left\{\tilde{Q}^o_{vB}(\bar{r}) + \tilde{Q}^o_{vA}(\bar{r})\cdot\left[\tilde{I} + \tilde{P}^o_{hB}(\bar{r}_A)\right]\right\} \cdot\left\{\tilde{I} + \tilde{P}^o_{hB}(\bar{r}) + \tilde{P}^o_{hA}(\bar{r})\cdot\left[\tilde{I} + \tilde{P}^o_{hB}(\bar{r}_A)\right]\right\}^{-1} \quad (72)$$

Equation (51) of the EM scaling concepts discussed earlier indicates that scattered H-field tensors $\tilde{Q}^o_{hA}(\bar{r})$ and $\tilde{Q}^o_{vA}(\bar{r})$ of the smaller structure will be of lesser size than $\tilde{Q}^o_{hB}(\bar{r})$ and $\tilde{Q}^o_{vB}(\bar{r})$ of the larger structure in equation (71) at all but high frequencies where the larger structure is not responding. Hence, near-surface geological noise should not seriously affect estimates of $\tilde{K}_z(\bar{r})$ due to a buried target, provided the sizes of the noise and target structures are sufficiently different. Assessment of what constitutes sufficiently different sizes requires computer simulation of MT responses of specific inhomogeneities, such as we present shortly.

However, the electric field distortion from current-gathering in geological noise has a profound effect on the magnitudes of elements of $\tilde{Y}_z(\bar{r})$ since, as explained previously with the coupled body impedance, $\tilde{P}^o_{hA}(\bar{r})$ may be as great as $\tilde{P}^o_{hB}(\bar{r})$ near the geological noise, even at low frequencies. This analysis overrules the suggestion of equation (57), which ignored coupling between bodies, that the admittance response of small structures would be dwarfed by that of large structures. Also, as with $\tilde{Z}(\bar{r})$ in (65), coordinate directions must be selected so that $\tilde{P}^o_{hB}(\bar{r}_A)$ of (72) is nearly diagonal to avoid substantial disruption of target vertical admittance phases by the geological noise.

THREE-DIMENSIONAL MAGNETOTELLURIC MODEL STUDY

The theoretical concepts we have developed are now applied to specific resistivity inhomogeneities, of which two special classes are examined here. The first is comprised of small-scale, near-surface bodies, which represent geological noise. Only by a thorough cataloging of the MT responses of such noise, with special attention paid to the frequency dependence of these responses, can the distortions of deep target signatures due to geological noise predicted by our theoretical discourse be circumvented. The second class of bodies examined are also near-surface, but are of a much larger scale. These are meant to represent sedimentary basins, which can sometimes be targets of one's investigations while at other times are of only secondary interest. In the course of studying both classes of resistivity structure, we will address the second major purpose stated in the introduction to this paper, namely to establish the applicability of 1-D and 2-D algorithms for modeling 3-D observations.

The following MT responses were computed using the algorithm of Wannamaker and Hohmann (1982), capable of modeling 3-D bodies in arbitrarily layered hosts, with plane wave incident fields. This algorithm is an extension of that developed by Ting and Hohmann (1981), which simulates the MT responses of 3-D structures in uniform half-spaces. As per Jones and Vozoff (1978), MT quantities are derived from total fields computed using two independent polarizations of $\vec{E}_i^o$. All

calculations in the study were performed on the Prime 400 Series minicomputer of the Earth Science Laboratory/University of Utah Research Institute.

The Response of Small-Scale Structures

Geological noise is often of a much smaller scale than one's station spacing and thus presents a grave sampling problem for MT measurements. For example, the shallow hydrothermal alteration characteristic of geothermal resource areas of the western United States (Ward et al., 1978) can be extremely variable over distances of only a few hundred meters, and often resides directly over the hot brine reservoir or deep heat source constituting the targets of interest. Even if present 3-D modeling algorithms could accommodate such complex heterogeneity, which they cannot, it would be prohibitively expensive to record sufficient MT data to delineate its response. It hence becomes imperative to discriminate against geological noise by making increased use of MT quantities that are relatively insensitive to the noise.

Our model of near-surface, conductive geological noise appears in Figure 3 as a small prism, 600 m by 300 m by 300 m with a depth to top of 25 m. The 4 Ω-m body is enclosed in a 400 m thick, moderate contrast layer of 40 Ω-m resistivity overlying a 400 Ω-m basement. The scattering current within the body was approximated by 48 rectangularly prismatic cells to a quadrant. Contoured MT quantities shown next, with coordinate axes paralleling the axes of symmetry of the body, were derived from 92 variously spaced receiver points per quadrant and required about 4 hours CPU time for each frequency on the Prime 400.

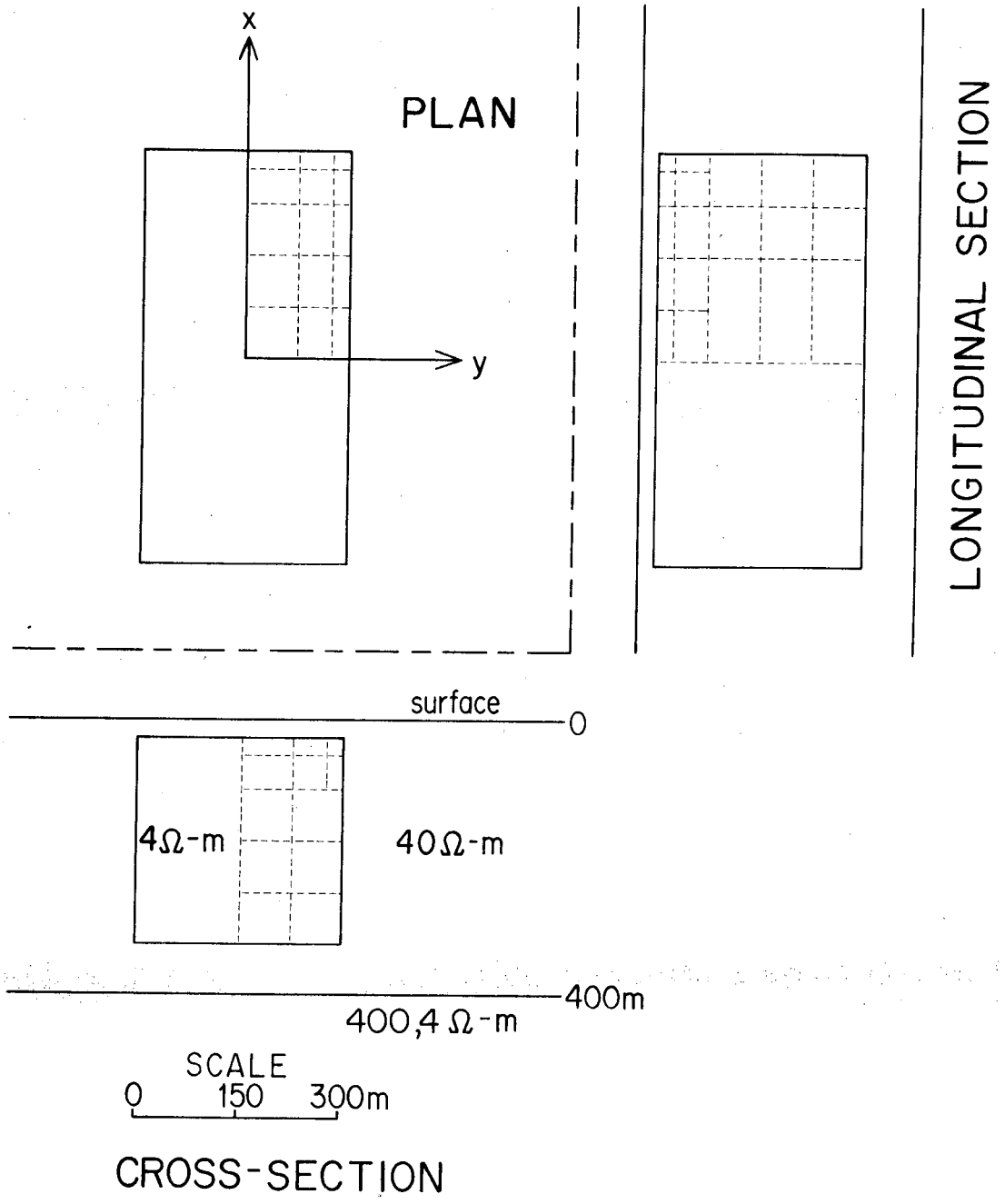

Figure 3. Prismatic 3-D body in a two-layered earth used to represent small-scale, shallow geological noise. Dashes outline the discretization of the conductor into rectangular cells, shown only for the right half of the body in section and the upper right-hand quadrant in plan. Basal half-space resistivities of 400 and 4 Ω-m are considered.

Apparent Resistivities and Impedance Phases. - The apparent resistivity signatures produced by our model of geological noise are displayed in Figure 4. Especially at the lower frequencies of 1. and 10 Hz where equation (33) becomes accurate and current-gathering is of particular importance, the anomalies are roughly electric dipolar in nature (Stratton, 1943, p. 431-434, p. 563-573), with undershoots and overshoots with respect to ρ_ℓ occuring over the ends of the body for ρ_{xy} and over the sides for ρ_{yx}. Note also at the lower frequencies that the anomalies are greater than those at 100 and 1000 Hz. Boundary polarization charges cause apparent resistivities to vary spatially by a factor of nearly 100, which is much higher than the body-host layer contrast, although such extremes are due partly to the abrupt nature of the resistivity contacts of the model and may be subdued for diffuse boundaries. It is most important, however, to realize that current-gathering in geological noise similar to our model will produce strong apparent resistivity anomalies that actually increase to a low frequency asymptote as frequency falls. The results complement the study of Berdichevsky and Dmitriev (1976), who considered a great variety of elliptically-shaped, near-surface inhomogeneities but who confined their attention to only the low-frequency limits of the distortions due to such inhomogeneities.

Behavior of the impedance phase is entirely different from that of the apparent resistivities, as seen in Figure 5. At 100 and 1000 Hz, departures may appear in excess of 20° from the layered host phase ϕ_ℓ, which is labeled in the upper right corner of each panel of the figure. At 1. Hz, on the other hand, the secondary electric field is essentially in phase with the incident $\vec{E}$-field and the total and

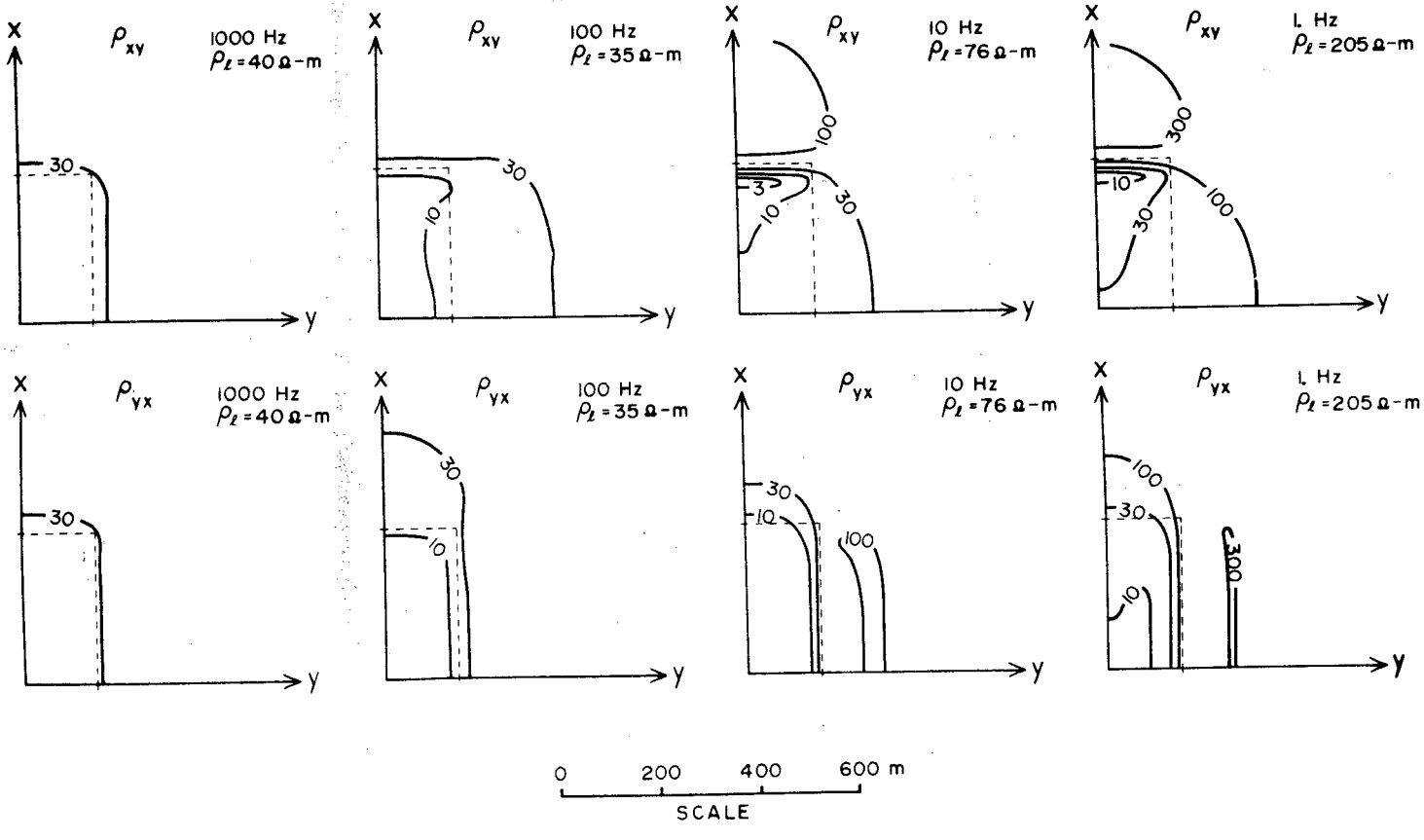

Figure 4. Multifrequency plan maps of tensor apparent resistivities ρ_{xy} and ρ_{yx} over upper right-hand quadrant of the inhomogeneity of Figure 3. The body outline in plan is shown with dashes, the basal half-space resistivity is 400 Ω-m and contour values are in Ω-m. Also, the frequency and the value of the layered earth apparent resistivity ρ_ℓ are given in the upper right-hand corner of each plot.

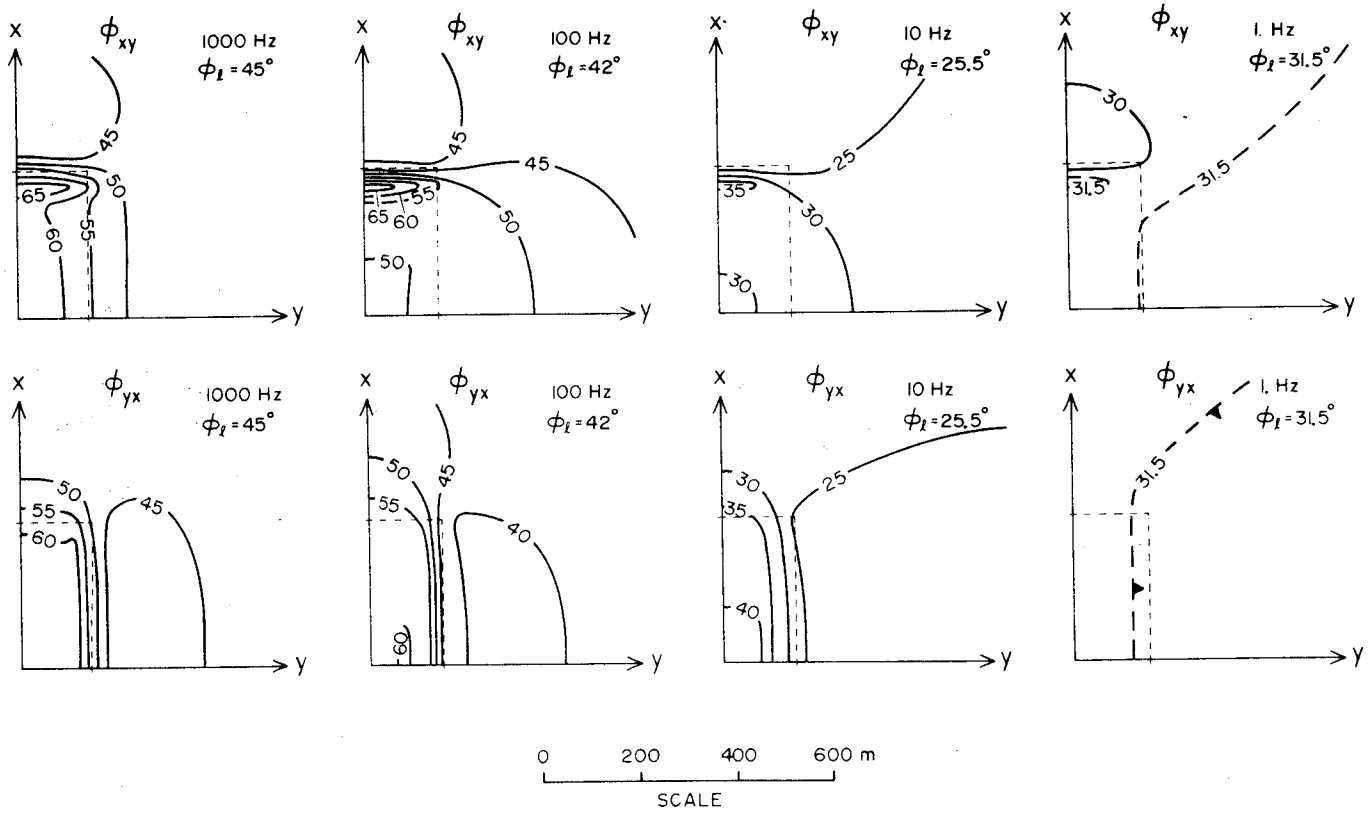

Figure 5. Multifrequency plan maps of tensor impedance phases ϕ_{xy} and ϕ_{yx} over upper right-hand quadrant of the inhomogeneity of Figure 3. The body outline in plan is shown with dashes, the basal half-space resistivity is 400 Ω-m and contour values are in degrees. Also, the frequency and the value of the layered earth impedance phase ϕ_ℓ are given in the upper right-hand corner of each plot.

incident H-fields are very nearly equal, so that impedance phase values deviate less than 3° from ϕ_ℓ. Impedance phase anomalies due to our model of small-scale geological noise peak at high frequencies, certainly in excess of 100 Hz, and contribute negligibly to observed phase responses below 1. Hz.

Vertical Magnetic Field Functions. - Peak amplitudes of around 0.15 for $|K_{zx}|$ and 0.20 for $|K_{zy}|$ at 100 and 1000 Hz over this conductor are illustrated in Figure 6. At 1. Hz, because of the appearance of $\tilde{Z}_\ell$ in (40), values of $|K_{zy}|$have decreased markedly and barely reach 0.10. Complicated anomalies in the phase of elements of $\tilde{K}_z(\bar{r})$ are seen in Figure 7 at 100 and 1000 Hz. At distance from the body at these higher frequencies, the rather uniform spacing of the phase contours represents an outwardly propagating secondary wavefront from this essentially electric dipole scatterer. Beyond several hundred meters, however, the contour spacing broadens, indicating we are approaching the far-field where secondary wavefronts become transverse electromagnetic (TEM) to z. Phases at 1. Hz, as foretold by equation (40), have approached the layered earth impedance phase $\phi_\ell = 31.5°$. In conclusion, responses in both magnitude and phase of elements of $\tilde{K}_z(\bar{r})$ due to this sort of geological noise are most important at frequencies above 100 Hz, leaving the signatures of any larger or deeper target relatively uncontaminated at lower frequencies.

Figure 8 shows $|Y_{zx}|$ and $|Y_{zy}|$ peaking at 1. Hz, since $\tilde{P}^o_s(\bar{r})$ and $\tilde{Q}^o_s(\bar{r})$ approach a maximum for this short 3-D body at low frequencies. The large values just inside prism corners are mostly due to $\det[\tilde{I} + \tilde{P}^o_h(\bar{r})]$ becoming very small, and are perhaps infrequent over more

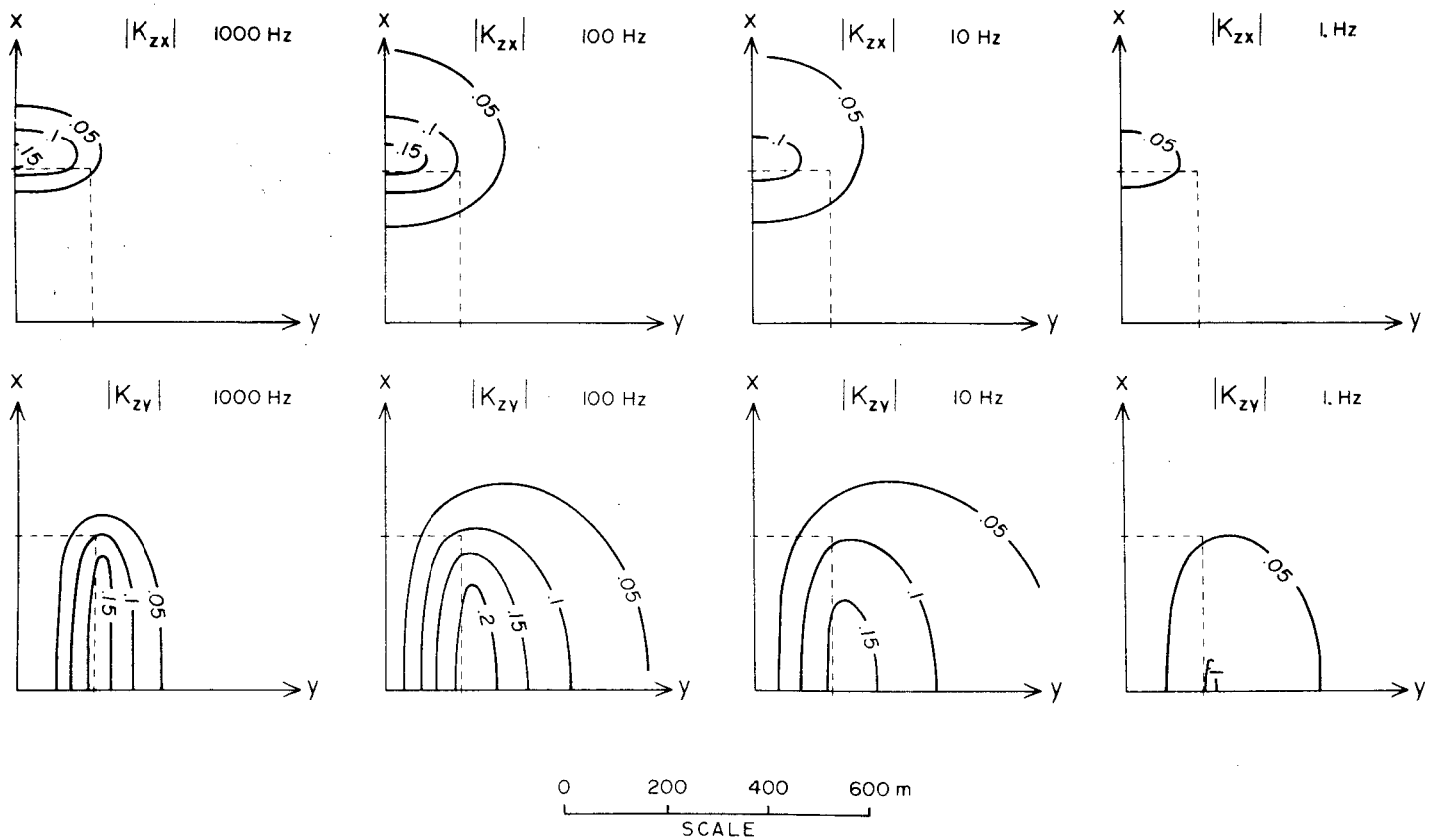

Figure 6. Multifrequency plan maps of tipper element magnitudes $|K_{zx}|$ and $|K_{zy}|$ over upper right-hand quadrant of the inhomogeneity of Figure 3. The body outline in plan is shown with dashes, the basal half-space resistivity is 400 Ω-m and contour values are dimensionless.

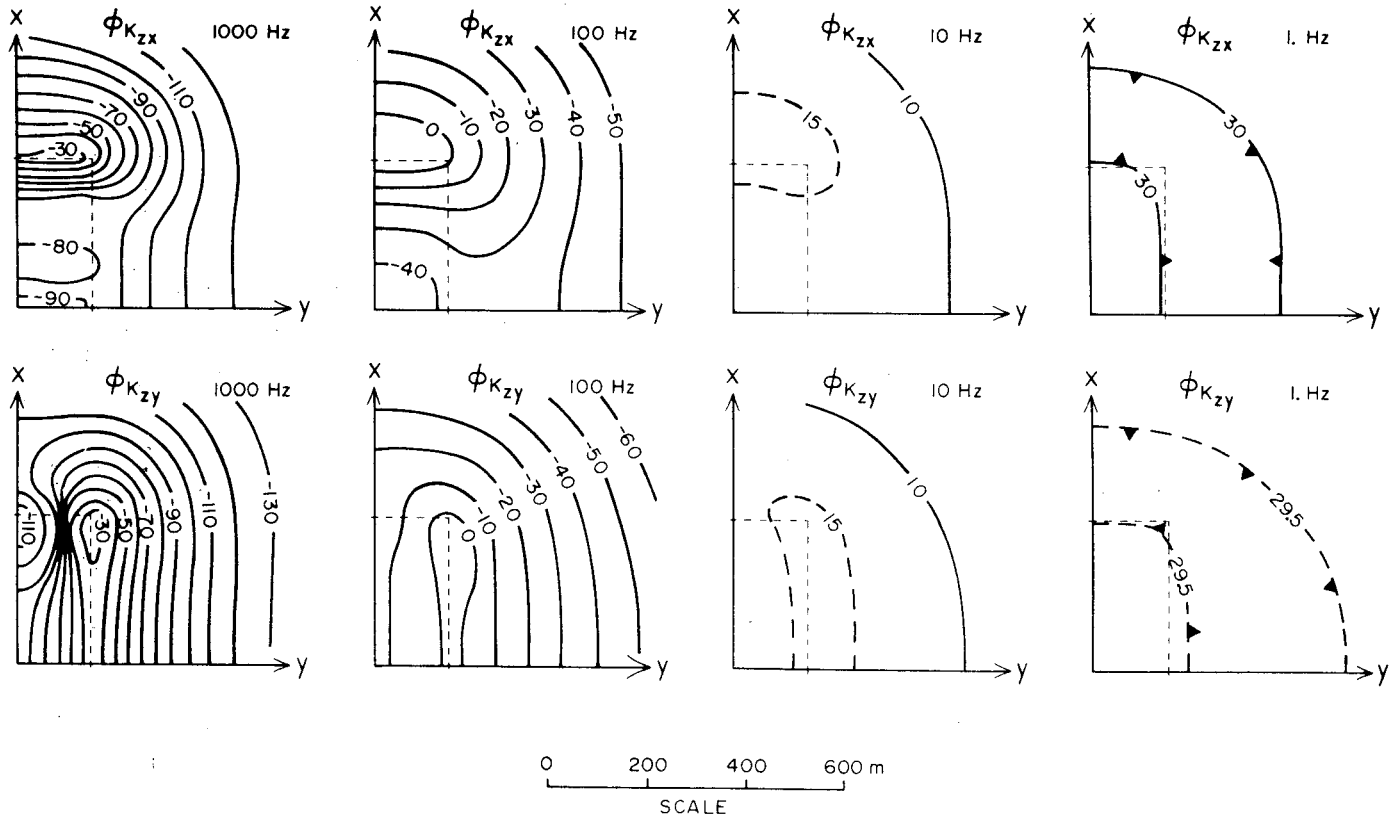

Figure 7. Multifrequency plan maps of tipper element phases over upper right-hand quadrant of the inhomogeneity of Figure 3. The body outline in plan is shown with dashes, the basal half-space resistivity is 400 Ω-m and contour values are in degrees.

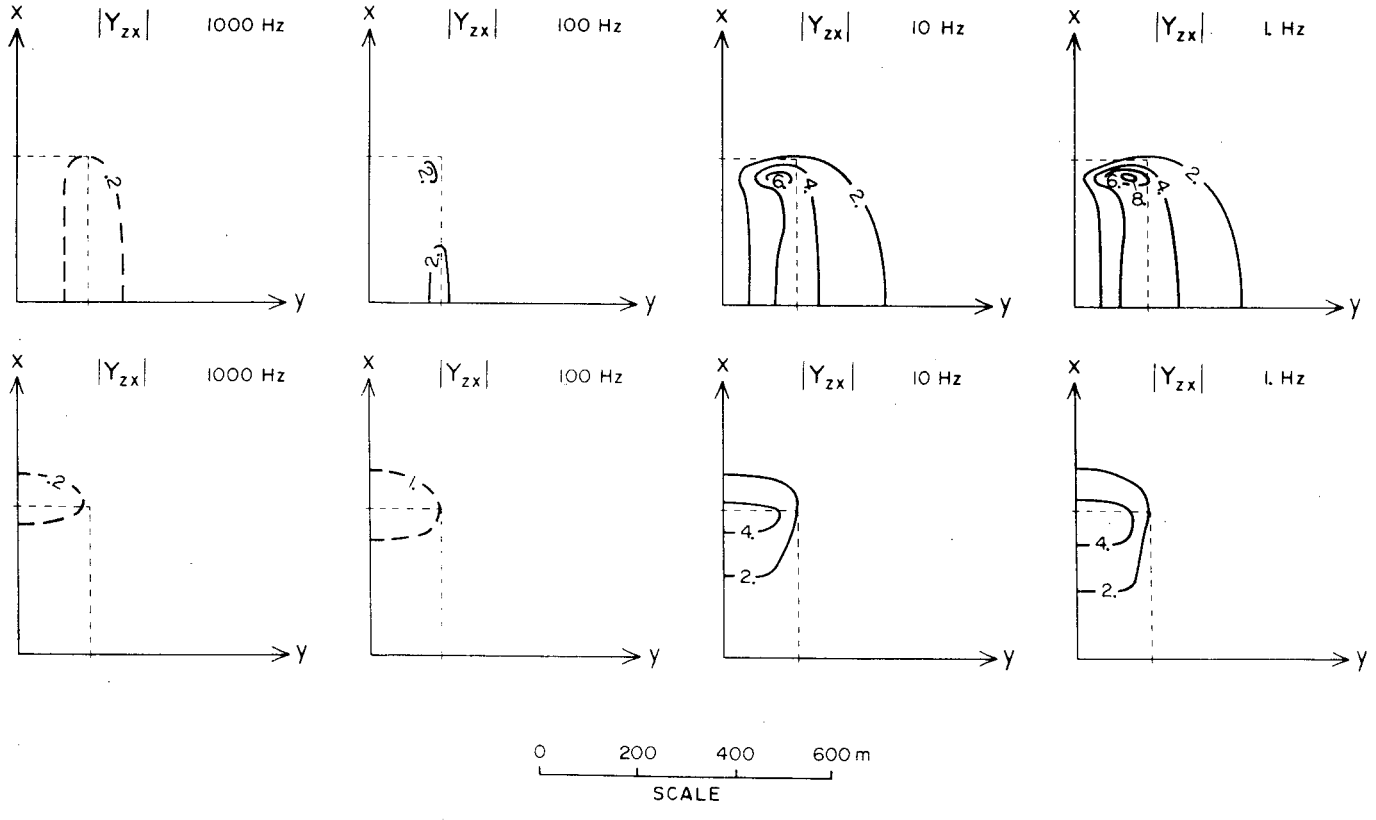

Figure 8. Multifrequency plan maps of vertical admittance element magnitudes $|Y_{zx}|$ and $|Y_{zy}|$ over upper right-hand quadrant of the inhomogeneity of Figure 3. The body outline in plan is shown with dashes, the basal half-space resistivity is 400 Ω-m and contour values are in Seimens (S).

diffuse resistivity structure. Nevertheless, as was the case for the apparent resistivities, geological noise causes strong anomalies in magnitudes of vertical admittance elements that increase to some low-frequency limit as frequency falls. The variation of phases in Figure 9 at distance from the inhomogeneity at 100 and 1000 Hz is again indicative of outwardly propagating secondary wavefronts while at 1. Hz, consistent with (41), vertical admittance phase has reduced to near zero for Y_{zx} and 180° for Y_{zy}, and is not affected in any important manner by the geological noise.

Figures 10 and 11 illustrate the role of the layered host in $\tilde{K}_z(\bar{r})$ and $\tilde{Y}_z(\bar{r})$. At 100 and 1000 Hz, anomalies in tipper for a conductive basement of 4 Ω-m are essentially identical to those for a resistive basement of 400 Ω-m, since at these high frequencies, $\tilde{Q}_s^o(\bar{r})$ and $\tilde{Z}_\ell$ are insensitive to ρ_2. Significant differences are apparent at 1. Hz, however, with peak anomalies for ρ_2 = 400 Ω-m being greater by a factor of about 4 1/2 than those for ρ_2 = 4 Ω-m. This factor is close to the ratio of the layered earth impedance magnitudes at 1. Hz for the two hosts, as explained by equation (40). One dimensional hosts with layer resistivities that increase with depth, through their effect on $\tilde{Z}_\ell$ as discussed with equation (28), tend to prolong the anomalies in $\tilde{K}_z(\bar{r})$ to lower frequencies than do layered hosts that become more conductive with depth.

In Figure 11, anomalies in the vertical admittance function A of equation (44) are rather similar for the two basements at all frequencies. This is consistent with the definition of A in (44), which does not involve $\tilde{Z}_\ell$. A 25% discrepancy between values using the two

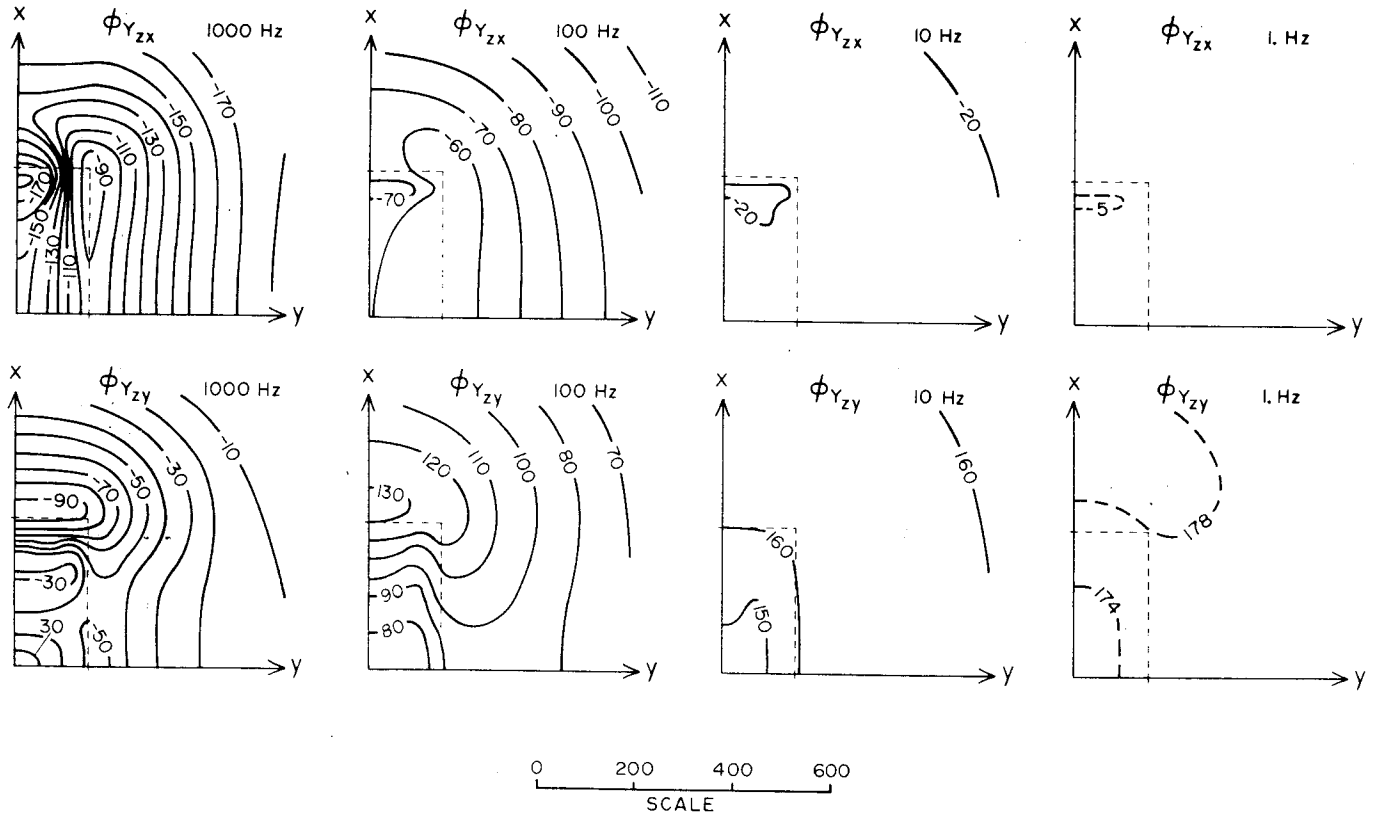

Figure 9. Multifrequency plan maps of vertical admittance element phases over upper right-hand quadrant of the inhomogeneity of Figure 3. The body outline in plan is shown with dashes, the basal half-space resistivity is 400 Ω-m and contour values are in degrees.

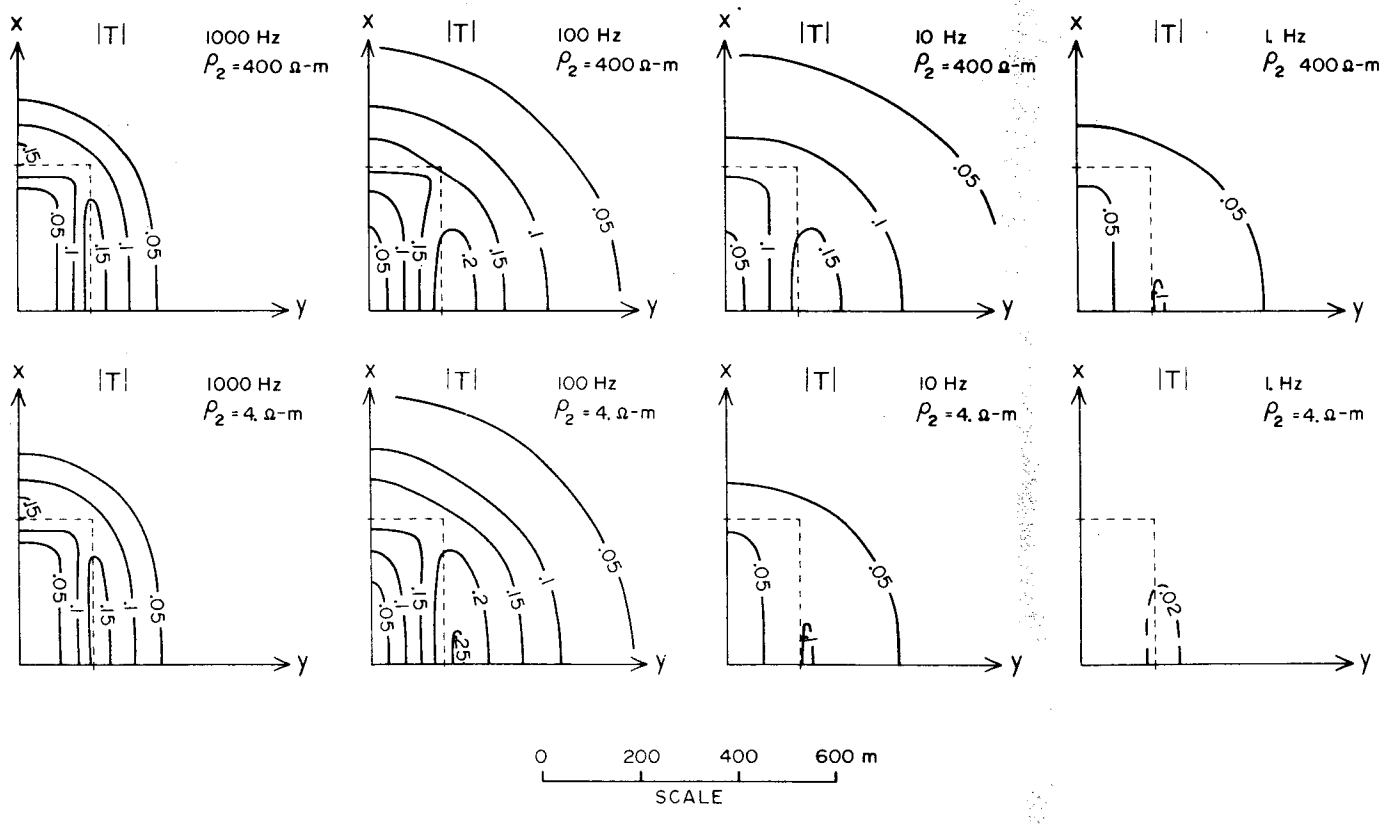

Figure 10. Multifrequency plan maps of tipper magnitude |T| over upper right-hand quadrant of the inhomogeneity of Figure 3. The body outline is shown in plan with dashes and the contours are dimensionless. Basal half-space resistivities of 400 and 4 Ω-m, identified in the upper right-hand corner of each plot, have been considered in the upper and lower rows of diagrams.

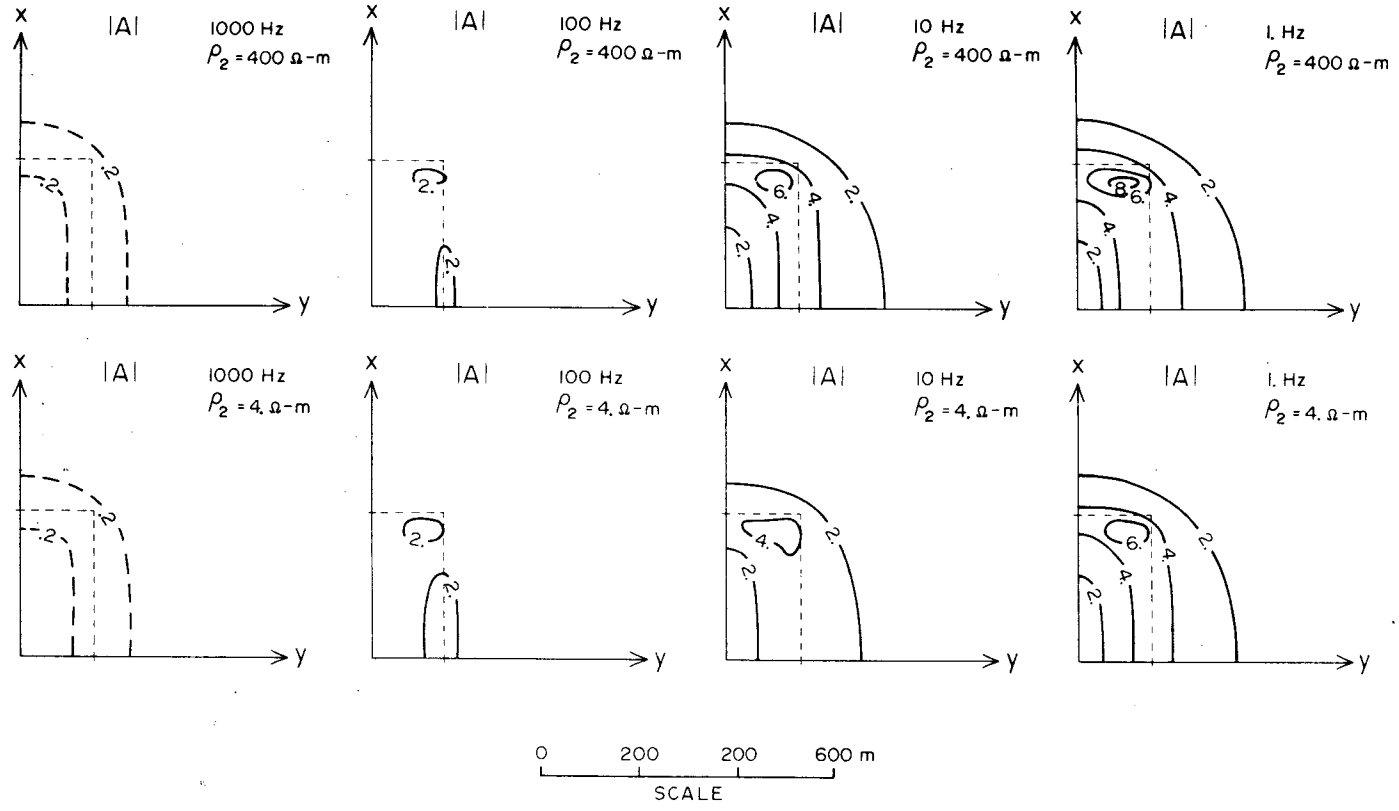

Figure 11. Multifrequency plan maps of vertical admittance function magnitude |A| over upper right-hand quadrant of the inhomogeneity of Figure 3. The body outline is shown in plan with dashes and the contours are in S. Basal half-space resistivities of 400 and 4 Ω-m, identified in the upper right-hand corner of each plot, have been considered in the upper and lower rows of diagrams.

basements is evident at 1. Hz, indicating the degree to which $P_s^o(\bar{r})$ and $Q_s^o(\bar{r})$ can be sensitive to the host layering for this 3-D geometry.

The Response of Sedimentary Basins

Porath (1971a) warned sternly of the effects that sedimentary basins could have upon MT measurements. Nowhere is this problem expected to be worse than in the Basin and Range tectonic province of the western United States, an area of pronounced horst-graben development since mid-Miocene time (Eaton, 1982). In light of the vigorous exploration for geothermal resources in this province, a thorough understanding of the consequences on MT measurements of these large-scale inhomogeneities is imperative. Also, from the ongoing tectonism has evolved a pronounced regional resistivity profile determined by a variety of physio-chemical mechanisms that is close to one-dimensional to depths exceeding 40 km (Brace, 1971). The role of this 1-D host in constraining secondary field distributions around the sedimentary basins is a further important variable to be quantified.

We have simulated a typical accumulation of graben alluvial fill, which often contains large amounts of conductive Pleistocene lacustrine clays (Hintze, 1980), by a large plate-like inhomogeneity (Figure 12). The physical properties of this prism are 36 km length, 14 km width, 1 km thickness and 2 Ω-m resistivity. Although outcropping in nature, this valley model is buried 500 m to obtain accurate results with the integral equations algorithm. A four-layered host, representing a regional resistivity profile proposed for this tectonic province by Brace (1971), is also illustrated in Figure 12. Starting from the surface we have ρ_1 = 400 Ω-m (d_1 = 2 km), ρ_2 = 4000 Ω-m (d_2 = 15 km),

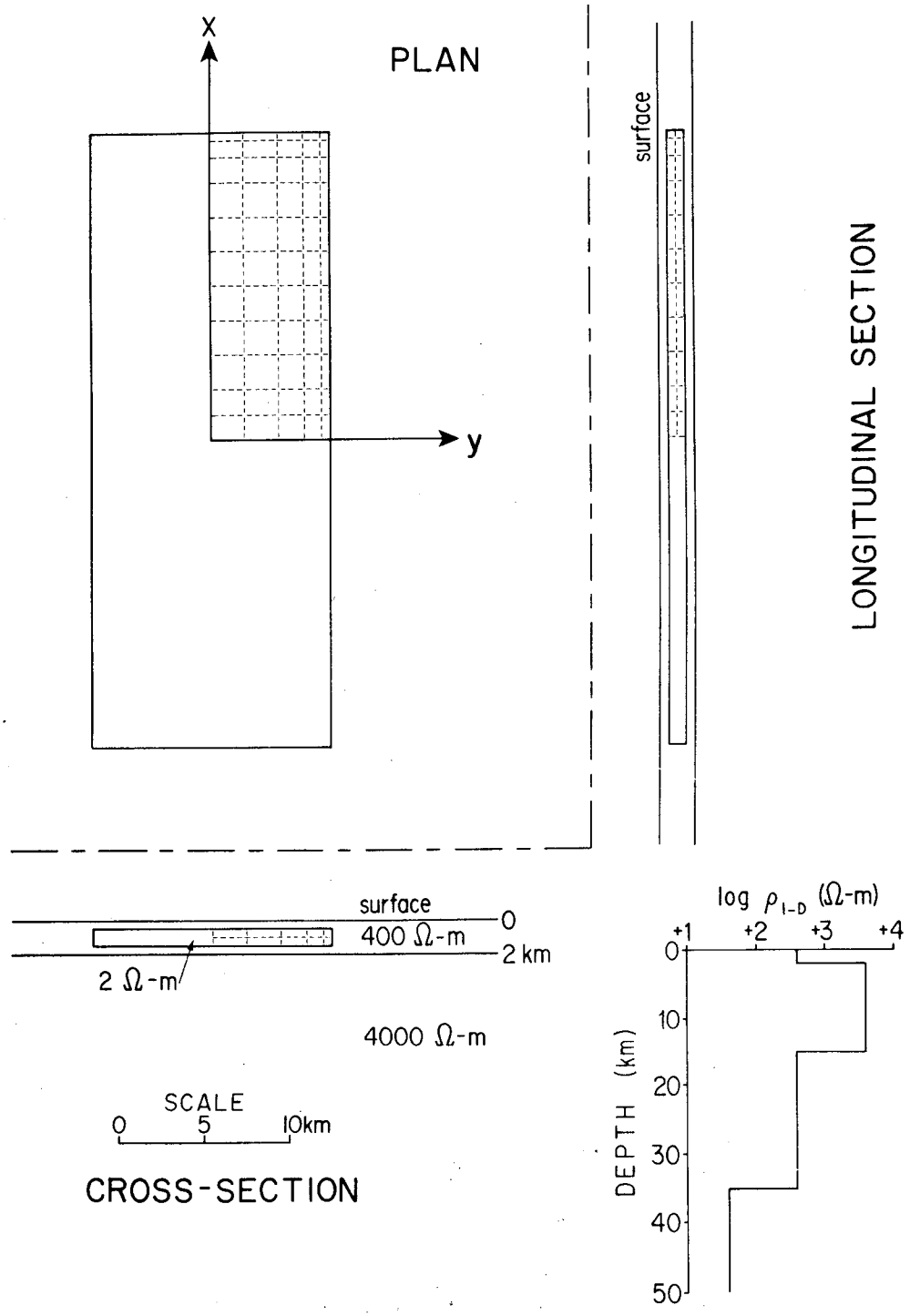

Figure 12. Platelike 3-D body in a four-layered earth representing a typical sedimentary basin in the Basin and Range tectonic province of the western United States. Dashes outline the discretization of the conductor into rectangular cells, shown only for the right half of the body in section and the upper right-hand quadrant in plan.

ρ_3 = 400 Ω-m (d_3 = 35 km) and a basal half-space ρ_4 = 40 Ω-m.

The scattering current in this model was approximated by 110 rectangularly prismatic cells in a quadrant and as many as 195 receiver points per quadrant were used to construct upcoming plots. Results required about 20 hours CPU time for each frequency on the Prime 400.

Regional Current-Gathering. - In an initial effort to illustrate the consequences of sedimentary basins upon MT observations, we study the widespread distortion of electric fields in their vicinity. Figures 13 and 14 contain plan views of total electric field polarization ellipses at 0.032 Hz over one quadrant of the basin for x- and y-directed polarizations of $\vec{E}_i^o$. This is a fairly low frequency for this scale of structure and the response is largely near-field or galvanic, so the ellipses are almost linear.

A clear display of regional current-gathering appears in Figure 13, showing the undershoot to overshoot, electric dipolar behavior of the ellipses expected over the end of a 3-D body for this orientation of $\vec{E}_i^o$. With the incident field directed along the x-axis, a regional depression of $\vec{E}_t^o(\bar{r})$ occurs to the side of the basin in the y-direction. Outside the corner of the prism, very large values of $\vec{E}_t^o(\bar{r})$ occur, locally exceeding twice the incident $\vec{E}$-field and indicating current convergence from a large volume of the host to the smaller end of the basin.

The electric field ellipses in Figure 14 for a y-oriented incident $\vec{E}$-field show behavior complementary to those in Figure 13. The electric dipolar character of the ellipses is evident over the side of the body

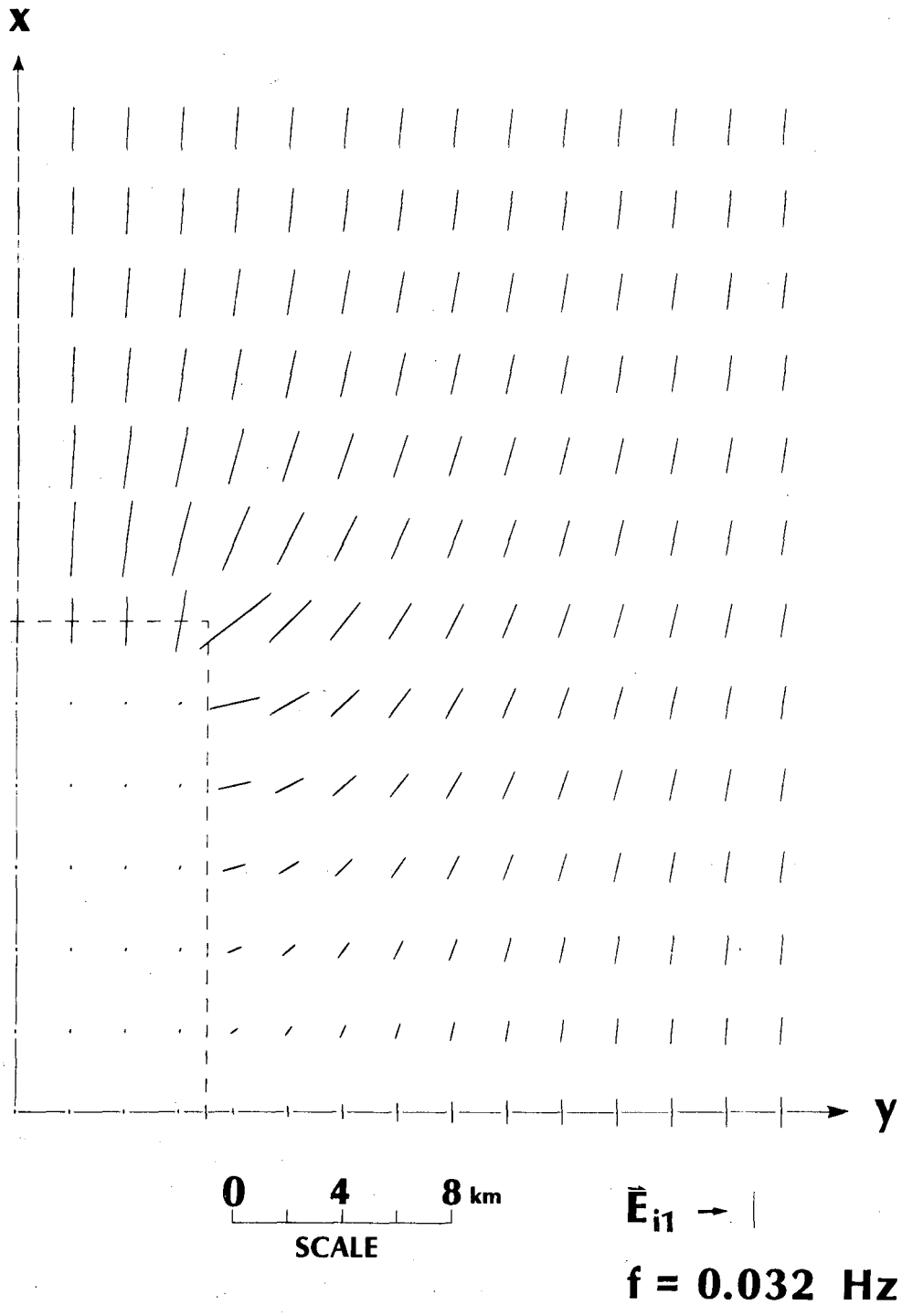

Figure 13. Plan view of total $\vec{E}$-field polarization ellipses over upper right-hand quadrant of basin model at 0.032 Hz for an x-directed incident field. The magnitude of the linearly polarized $\vec{E}_i^0$ is shown in the lower right-hand corner of the diagram.

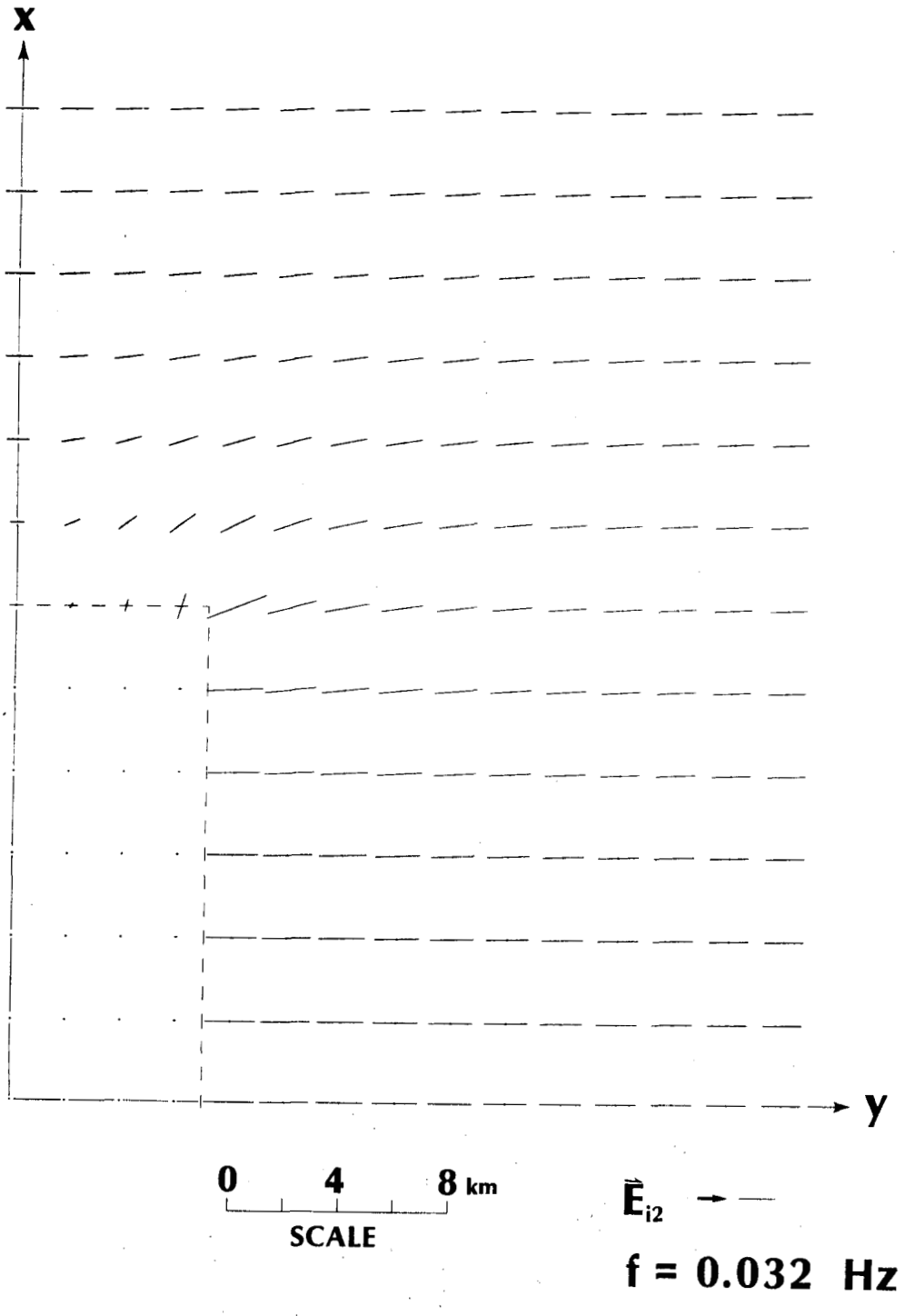

Figure 14. Plan view of total $\vec{E}$-field polarization ellipses over upper right-hand quadrant of basin model at 0.032 Hz for a y-directed incident field. The magnitude of the linearly polarized $\vec{E}_i^0$ is shown in the lower right-hand corner of the diagram.

for this polarization of $\vec{E}_i^o$, in particular causing a regional amplification of $\vec{E}_t^o(\bar{r})$ to the side of the basin in the y-direction. Very small total $\vec{E}$-fields appear directly over the model for both polarizations of $\vec{E}_i^o$, with the y-directed incident field giving a somewhat more extreme anomaly.

Specific effects of the layering upon regional current-gathering can be demonstrated in section views. In Figure 15, the basin model resides in a uniform half-space of 400 Ω-m and total electric field polarization ellipses have been computed, again at 0.032 Hz, to a depth in excess of 20 km. The approximately electric dipolar character of $\vec{E}_t^o(\bar{r})$ in section is apparent, where boundary charges effect current from great depth gathering up to the valley and subsequently discharging from the far end. As in the plan views involving the layered host, very large values of total $\vec{E}$-field are seen near the ends of the plate. The under- to overshoot behavior of $\vec{E}_s^o(\bar{r})$ drawn at the top of the figure is another view of this phenomenon; at distances near 40 km from the prism's center, $|\vec{E}_s^o(\bar{r})|$ has decayed to about 5% of $\vec{E}_i^o$.

In Figure 16, the model is returned to its four-layered host and $\vec{E}$-field polarization ellipses are again calculated. In the uppermost 400 Ω-m layer containing the basin model the ellipses are very horizontal and attenuate with distance much more slowly than in the case of the half-space host. The plot of $\vec{E}_s^o(\bar{r})$ in the upper part of the figure supports this, with $|\vec{E}_s^o(\bar{r})|$ at distances near 40 km from the plate's center exceeding $|\vec{E}_i^o|$ by over 20%. To comprehend this relatively slow attenuation, one must realize that secondary currents induced in the 400 Ω-m layer about the basin have difficulty penetrating the more resistive

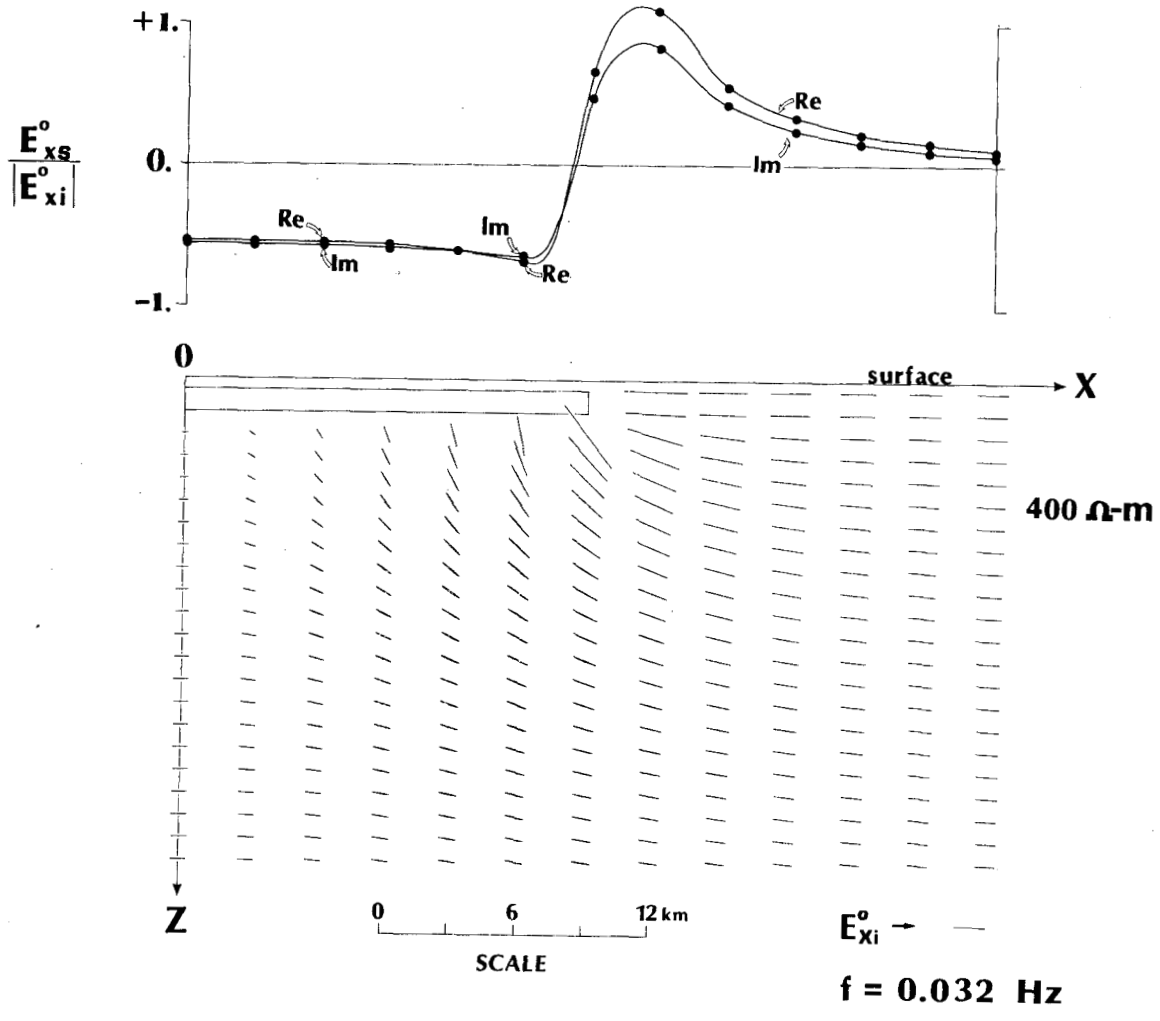

Figure 15. The basin model is enclosed in a 400 Ω-m half-space for this section view of total $\vec{E}$-field polarization ellipses through one half of the basin at 0.032 Hz. The incident field is linearly polarized in the x-direction and its magnitude at the surface is shown in the lower right-hand corner of the diagram. At the top of the figure are profiled real and imaginary components of $\vec{E}^o_s(\bar{r})$ normalized by $|\vec{E}^o_i|$.

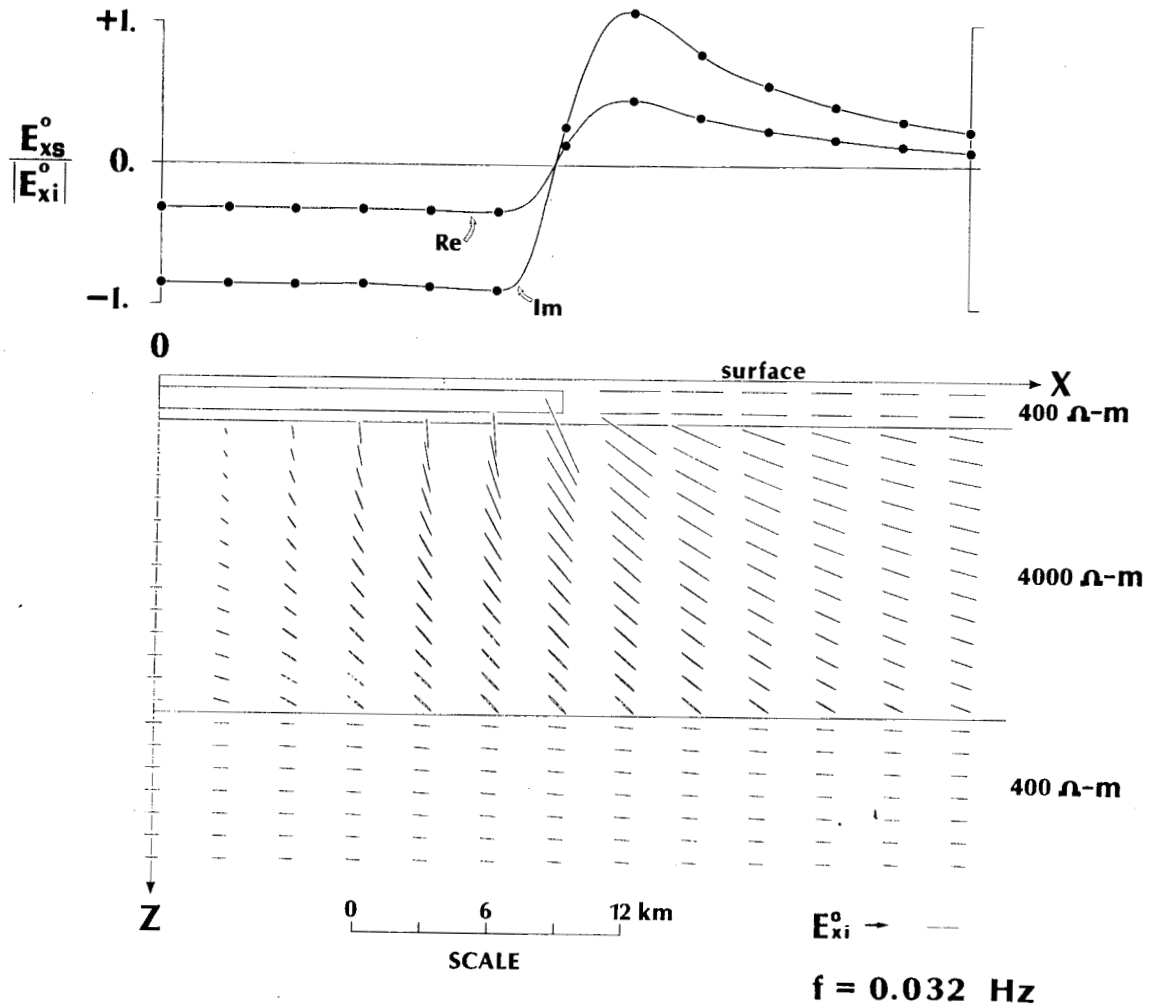

Figure 16. The basin model is returned to the four-layered host for this section view of total $\tilde{E}$-field polarization ellipses at 0.032 Hz. The incident field is again linearly polarized in the x-direction and its magnitude at the surface is shown in the lower right-hand corner of the diagram. At the top of the figure are profiled real and imaginary components of $\tilde{E}^o_s(\bar{r})$ normalized by $|\tilde{E}^o_i|$.

4000 Ω-m medium, and hence can decay geometrically mostly in just the x-y plane (Wannamaker and Hohmann, 1982). By contrast, secondary currents about the basin in the uniform 400 Ω-m half-space can die away readily in the z-direction as well. Hence, the surface anomaly in Figure 16 is observed to be important to greater distances from the body than is that in Figure 15.

However, despite the fact that secondary current flow about the basin in the four-layered earth has difficulty in penetrating the 4000 Ω-m medium, electric field ellipses in this most resistive layer in Figure 16 exhibit much stronger vertical components than those at comparable depths in the 400 Ω-m half-space in Figure 15. This phenomenon is due to the preservation of the normal component of current density across layer interfaces, which in turn means that the vertical component of secondary electric field experiences a step jump by a factor of ten going from the 400 Ω-m layer down to the 4000 Ω-m layer (note there is no vertical component of the primary field). Nevertheless, we emphasize that values of secondary current density in the 4000 Ω-m material are actually much smaller than values at corresponding positions in the less resistive, 400 Ω-m half-space host. This is clearly confirmed by the very flat nature of the ellipses in Figure 16 in the deep 400 Ω-m layer extending from 15 to 35 km, showing that deep regional current flow is essentially insulated by the 4000 Ω-m layer from the effects of the conductive basin.

Magnetotelluric Strike Estimations. - Principal coordinate directions of tensor MT quantities provide measures of preferred geoelectric orientations. All MT strike estimators, however, are not

equal in their ability to depict true earth resistivity trends or in their ability to distinguish preferred directions of target structure from preferred directions of geological noise.

In Figure 17 are plotted the direction at which $|K_{zy}|$ is maximized, called K_z-strike or tipper-strike, along with the principal axis of $\tilde{Z}(\bar{r})$ nearest K_z-strike, which we call Z-strike, for a variety of receivers at 0.032 Hz. Principal axes of $\tilde{Z}(\bar{r})$, which we define as coordinates maximizing $|Z_{xy}|$ and $|Z_{yx}|$ individually, occur every 90° so that they alone cannot give unique strike directions (Word et al., 1971).

Tipper-strike conforms more closely to the true limits, both sides and ends, of the valley than does Z-strike (Jones and Vozoff, 1978), though calculations not presented show each tends increasingly to parallel the boundaries of the model at higher frequencies. Z-strike also seems the less stable of the two estimators over the plate, where impedance anisotropy is relatively slight.

The orientations at which $|Y_{zx}|$ is maximized, called Y_z-strike, as well as strike directions based on maximizing the phase of an off-diagonal element of $\tilde{Z}(\bar{r})$, labeled ϕ-strike, have also been computed (Figure 18). For this valley model, Y_z strike and ϕ-strike are very similar to K_z-strike and Z-strike respectively, with ϕ-strike also possessing a 90° ambiguity if unconstrained.

Over single inhomogeneities such as that of Figure 12, we conclude that K_z-strike and Y_z-strike are somewhat superior to Z-strike and ϕ-strike due to their closer conformity to true geoelectric trends,

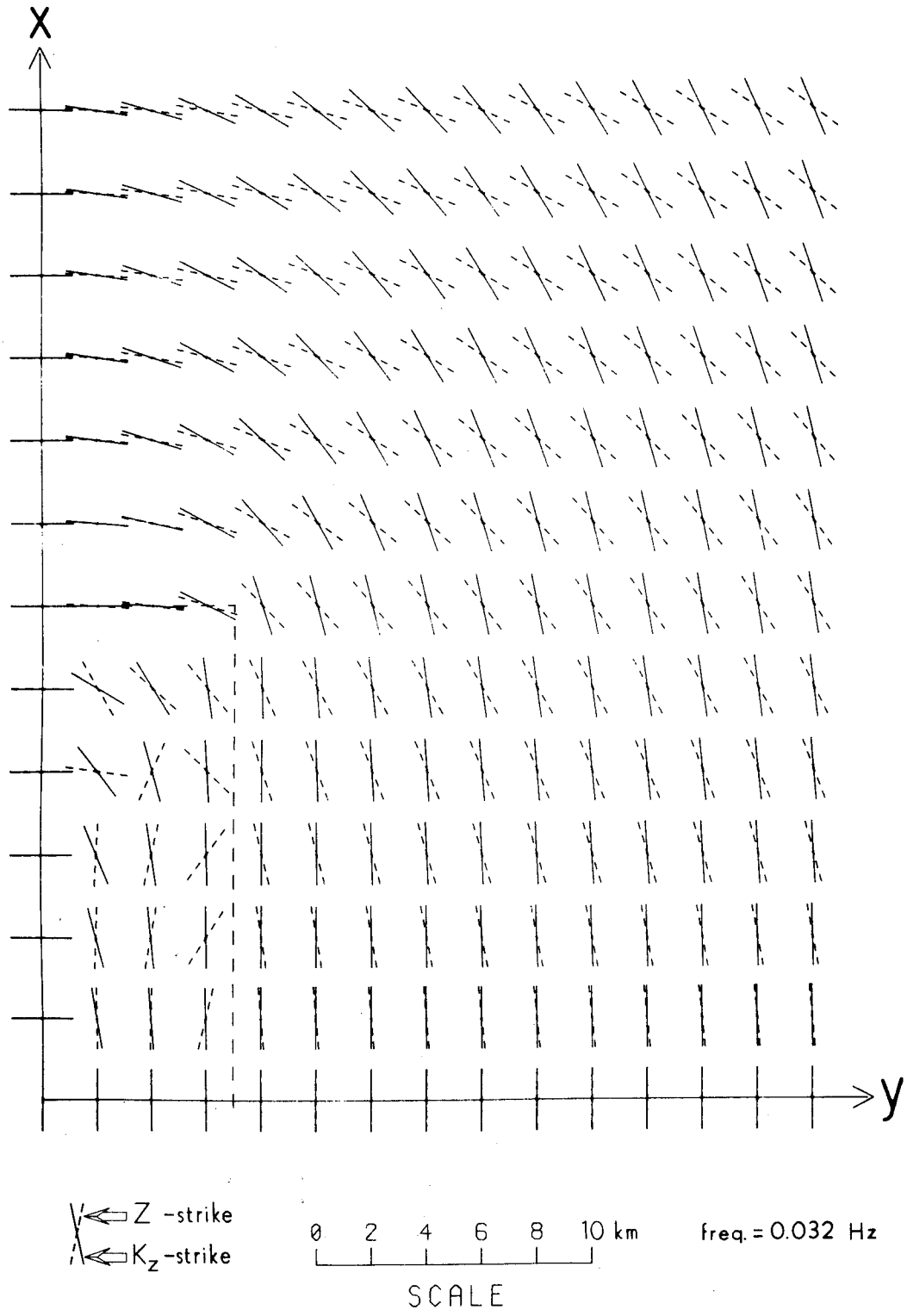

Figure 17. Plan view of MT strike estimators K_z-strike and Z-strike over the upper right-hand quadrant of the basin model for a variety of receivers at 0.032 Hz.

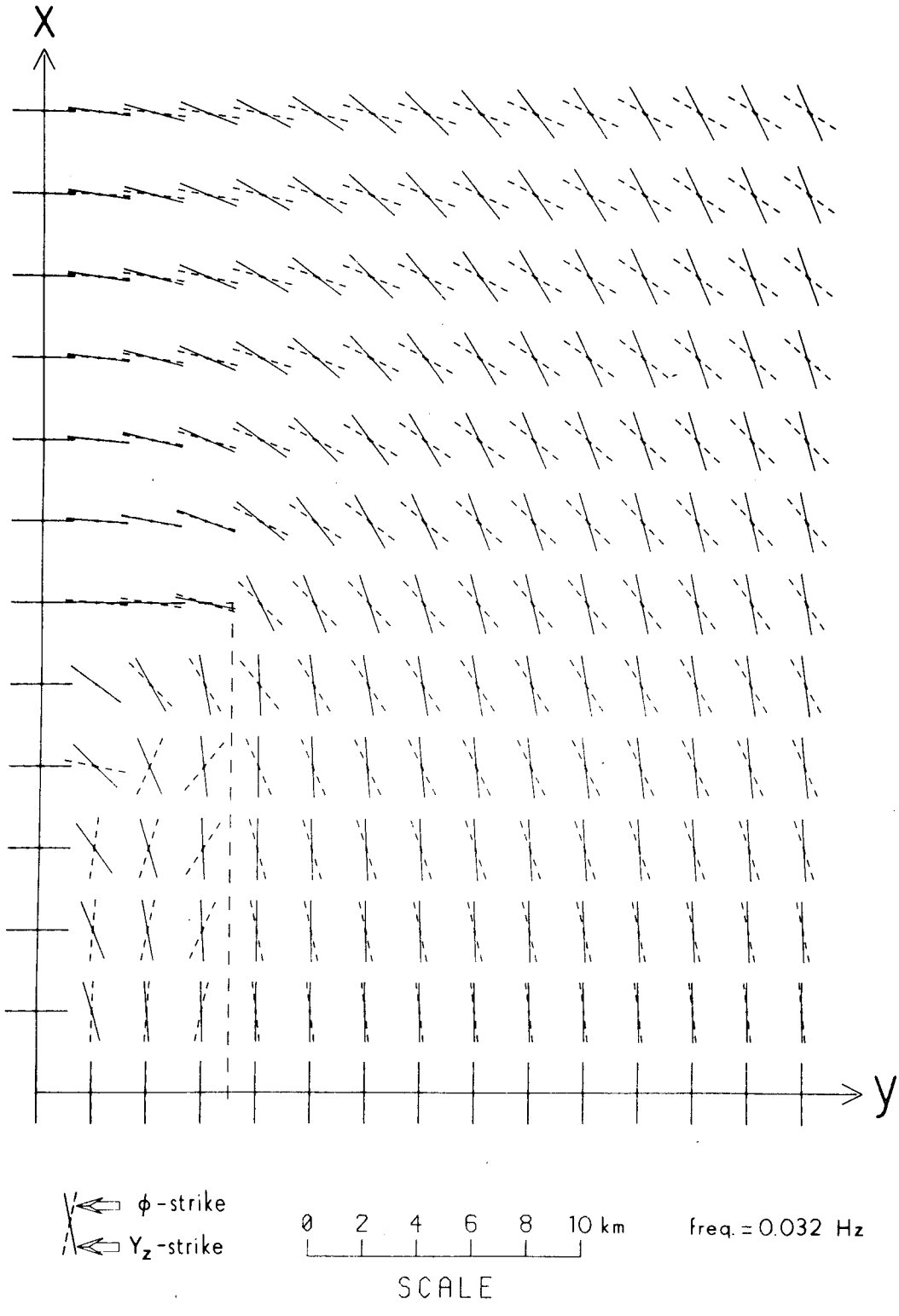

Figure 18. Plan view of MT strike estimators Y_z-strike and ϕ-strike over the right-hand quadrant of the basin model for a variety of receivers at 0.032 Hz.

their greater stability and their lack of a 90° ambiguity (compare Gamble et al., 1982). Nevertheless, all four estimates show reasonably close agreement overall, especially to the side of the valley, and thus are considered largely equivalent for single bodies.

However, the earlier coupled body theory indicates that Y_z-strike as well as Z-strike may be significantly distorted by current-gathering in near-surface geological noise. Equation (71), on the other hand, shows that tipper-strike is not affected in this manner. Furthermore, the same coupled body analysis can show that ϕ-strike also escapes serious disruption by geological noise. To demonstrate this, we note first that the similarity of Z-strike and ϕ-strike in Figures 17 and 18 indicates that principal axes of $\tilde{\tilde{P}}^{o}_{hB}(\bar{r})$ in (65) correspond closely to ϕ-strike. Second, we assume that $\tilde{\tilde{P}}^{o}_{hB}(\bar{r}_A) \simeq \tilde{\tilde{P}}^{o}_{hB}(\bar{r})$ in the vicinity of the geological noise and that the off-diagonal elements of $\tilde{\tilde{P}}^{o}_{hB}(\bar{r})$ are small compared to the diagonal elements of $\tilde{\tilde{P}}^{o}_{hB}(\bar{r})$ when this tensor is in its principal directions. If one then expands $\tilde{\tilde{Z}}(\bar{r})$ in (65) into its individual elements Z_{ij}, one will realize that any rotation of coordinate axes away from the principal directions of $\tilde{\tilde{P}}^{o}_{hB}(\bar{r})$ will only serve to de-extremize the phases of the coupled body impedance elements. Remember, though, that even if principal axes of target impedance phase are recoverable in the presence of geological noise, values of the coupled body impedance phases defined in coordinate directions other than the principal axes of $\tilde{\tilde{P}}^{o}_{hB}(\bar{r})$ will depart from values of the target impedance phases, as discussed with equation (65).

The upshot of the preceding paragraph is that K_z-strike and ϕ-strike are superior to Y_z-strike and Z-strike for estimating preferred

geoelectric trends in the face of small-scale, geological noise. In particular, K_z-strike and ϕ-strike can provide measures of the principal axes of $\tilde{P}^{o}_{hB}(\bar{r})$ in equations (65) and (72) due to a target buried beneath such noise. Hence, if data coordinates are defined using these two strike estimators, then impedance and vertical admittance phase responses due to a target may be recovered that are undistorted by current-gathering in small-scale, shallow inhomogeneities. Of these two estimators, we prefer tipper-strike for its lack of a 90° ambiguity and its greater reflection of true resistivity trends.

MT Quantity Pseudosections. - Detailed, multifrequency signatures of apparent resistivity, impedance phase, tipper and vertical admittance over our sedimentary basin model of Figure 12 are discussed in this final subsection. Our comprehension of the fundamental controls on 3-D MT anomalies, as well as the utility of 1-D and 2-D modeling algorithms in 3-D environments, develops to a maximum in this examination, and requires a fusion of previously developed concepts of current-gathering, electromagnetic scaling and coupled body responses.

Calculations were performed along two traverses over the 3-D valley model and are compared to calculations over a 2-D model of identical cross-section (Rijo, 1977; Stodt, 1978). All MT responses appear as pseudosections, in which log frequency and the y-axis serve as ordinate and abscissa for contour plots of amplitude and phase. The 3-D traverses reside along the line $x = 0$, over the prism's center, and along $x = 9$ km, half-way to the prism's end. For all results, MT quantity coordinates parallel plate symmetry axes.

Pseudosection contours were constructed from computations at every

half decade in frequency, from 0.001 Hz to 100 Hz. However, we distrust the numerical accuracy of the 3-D calculations above 10 Hz for this large body, although the discretization we have chosen is as fine as is practical with our computer. Since 3-D and 2-D values of all MT functions presented converge as frequency rises to 10 Hz, 3-D contours at higher frequencies were derived by extrapolation using 2-D results.

a.) Apparent Resistivities and Impedance Phases. - In Figure 19, agreement in ρ_{xy} and ϕ_{xy} between the profiles at x = 0 and x = 9 km over the 3-D body is close at all frequencies, but a significant departure from the 2-D transverse electric responses occurs below 1. Hz. The apparent resistivity over and adjacent to the 3-D plate, designated $\rho_{xy}(3\text{-D})$, decreases as frequency falls relative to the apparent resistivity of the layered host ρ_ℓ, which the 3-D response approaches at large distances from the valley. Correspondingly, anomalously high values of $\phi_{xy}(3\text{-D})$ appear in the vicinity of the body, although the discrepancy between this quantity and the host impedance phase ϕ_ℓ is less than 5° anywhere below 0.003 Hz. In contrast, $\rho_{xy}(2\text{-D})$ falls with respect to ρ_ℓ, while $\phi_{xy}(2\text{-D})$ surpasses ϕ_ℓ, only above 0.3 Hz, with just the opposite behavior at lower frequencies.

To understand this 3-D anomaly, consider the regional depression of $\vec{E}^o_t(\bar{r})$ occurring over and beside the valley when $\vec{E}^o_i$ is x-oriented (Figure 13). This depression, acting on ρ_{xy} through equations (31) and (33b), results overwhelmingly from boundary charges on the ends of the 3-D prism and reaches a maximum at low frequencies. Such current-gathering doesn't occur in the 2-D body for this transverse electric mode, so that the wave equation (7) approaches the homogeneous Laplace's

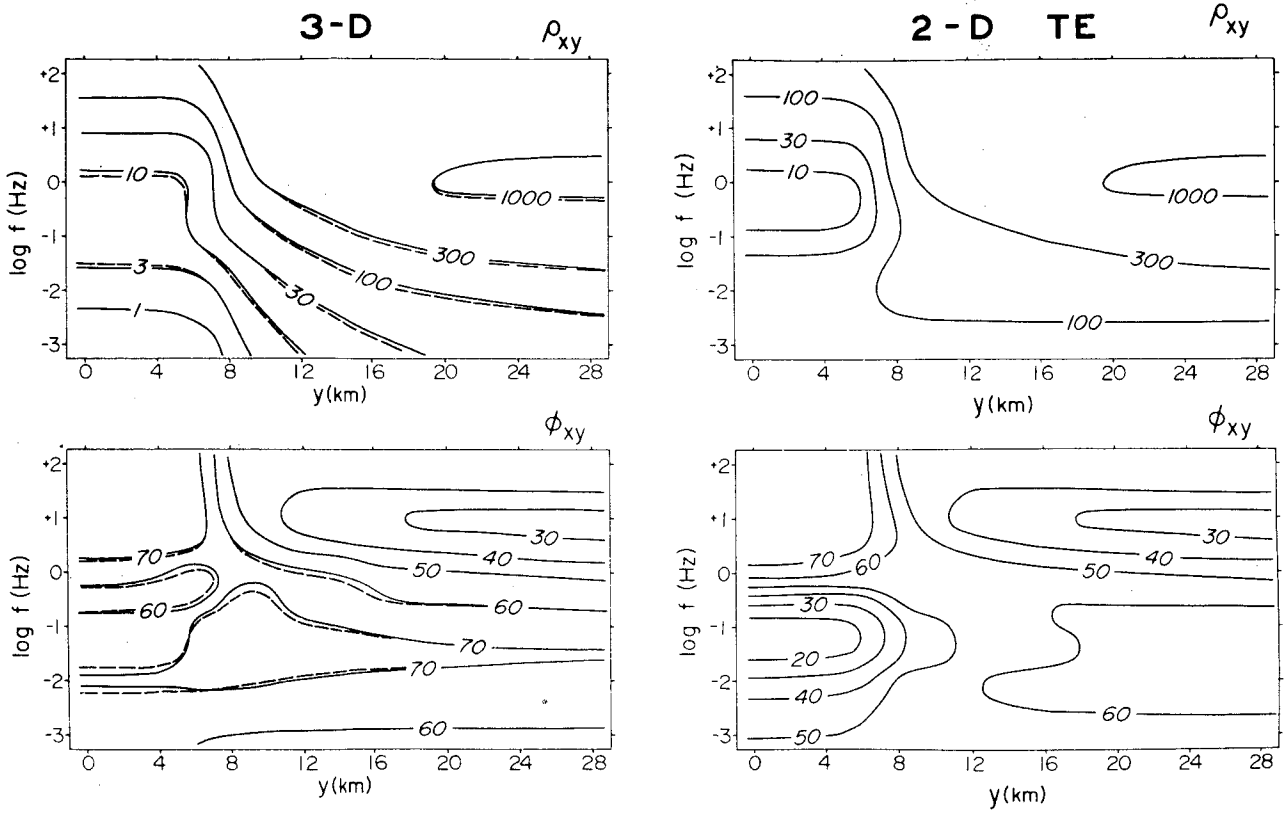

Figure 19. Pseudosections of ρ_{xy} and ϕ_{xy} for profiles at x = 0 (solid contours) and x = 9 km (dashed contours) over the 3-D basin model compared to 2-D TE pseudosections for corresponding model of infinite strike length. Pseudosections commence at y = 0 over the center of the basin and extend in the y-direction. Contours of ρ_{xy} and ϕ_{xy} are in Ω-m and degrees.

equation below 0.3 Hz and there is a diminishing contribution by the secondary $\vec{E}$-field to the anomalous ρ_{xy} and ϕ_{xy}. In fact, the 2-D TE responses at these lower frequencies result predominantly from a strong secondary $\vec{H}$-field, which remains important as governed by equations (20) and (31) until frequencies well under 0.001 Hz for the 2-D basin model. On the other hand, over the 3-D model at frequencies less than 0.3 Hz, $\tilde{H}_s^o(\bar{r})$ is much smaller than that over the 2-D counterpart. This is because boundary charges severely depress $\vec{J}_s$ within, and thus $\tilde{Q}_h^o(\bar{r})$ over, the 3-D body relative to the 2-D structure. Hence, ρ_{xy} and ϕ_{xy} for the 3-D basin model arrive at low frequency asymptotes around 0.003 Hz.

From Figure 19 we conclude that 2-D transverse electric modeling algorithms are of little value for interpreting apparent resistivities and impedance phases observed in regions of extensive lateral inhomogeneity such as the Basin and Range province. Indeed, even the limited conformity of 2-D TE and corresponding 3-D results we have shown is idealistic, since a sedimentary basin in nature is not uniform in cross-section along its strike extent. Furthermore, it is probable that 2-D TE routines will be totally inappropriate for interpreting MT measurements if small-scale geological noise such as we have simulated in Figure 3 is widespread.

In total contrast to the responses depicted in Figure 19, anomalies in ρ_{yx} and ϕ_{yx} in Figure 20 are essentially identical for the two 3-D traverses and the 2-D profiling. The reasons for this excellent agreement are twofold. First, no secondary $\vec{H}$-field exists for the 2-D TM mode (Swift, 1967), and there is only an insignificant contribution

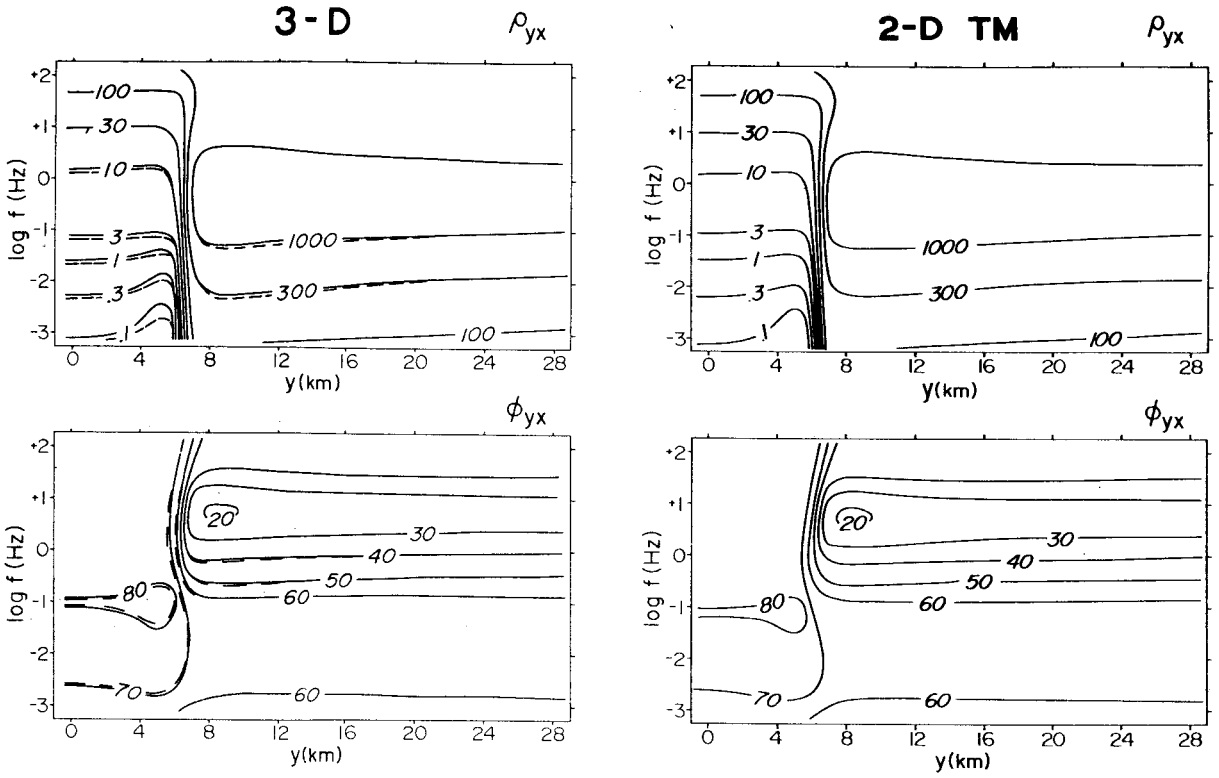

Figure 20. Pseudosections of ρ_{yx} and ϕ_{yx} for profiles at x = 0 (solid contours) and x = 9 km (dashed contours) over the 3-D basin model compared to 2-D TM pseudosections for corresponding model of infinite strike length. Pseudosections commence at y = 0 over the center of the basin and extend in the y-direction. Contours of ρ_{yx} and ϕ_{yx} are in Ω-m and degrees.

by $\vec{H}_s^o(\bar{r})$ to the corresponding 3-D response. Second, boundary charges on the sides of the basin are included in both 2-D TM and 3-D formulations. These boundary charges in turn lead to current-gathering into the sides of the 2-D and 3-D basin models. As was demonstrated for the 3-D model in Figure 14, such current-gathering is manifested in the development of a crudely dipolar variation in the electric field over the basin toward lower frequencies. It is this variation in the electric field which determines the apparent resistivity and impedance phase responses of Figure 20.

We infer, therefore, from Figure 20 that accurate models of earth resistivity may be interpreted from profiles of MT measurements across elongate 3-D bodies using a 2-D TM algorithm. In fact, the agreement between 2-D TM and corresponding 3-D responses for our sedimentary basin model remains excellent even at x = 12 km, which is quite close to the end of the model. From this it is presumed that the validity of a transverse magnetic modeling routine is not highly sensitive to variations in cross-section along the strike length of the 3-D inhomogeneity. Instead, interpretation using such an algorithm will yield a model resistivity cross-section which reflects mainly earth structure that is local to the specific profile being analyzed.

For this 2-D transverse magnetic approach to be successful, it is of great importance that the coordinate axes of the MT quantities be properly defined. We favor tipper-strike for specifying such coordinates, since it is a stable, unambiguous strike estimator that conforms closely to true geoelectric trends. Use of $\tilde{K}_z(\bar{r})$ to define MT quantity coordinate axes will result in pseudosections that are

essentially identical to those in Figures 19 and 20, with the possible exception of field points close to the center of the model whose axes may be constrained to be consistent with the majority of the strike estimates. In addition, our previous discussion of MT strike estimators points out that if data coordinate axes are defined using tipper-strike, then impedance phase responses due to a target may be recovered that are undistorted by current-gathering in small-scale, shallow geological noise, provided that tipper-strike can be calculated at frequencies for which the response in $\tilde{K}_z(\bar{r})$ due to the target is strong while the response due to the noise has attenuated.

It should be pointed out that use of a 2-D transverse magnetic algorithm as we propose it is no interpretive panacea. For example, consider a buried 3-D dike-like inhomogeneity elongated in the x-direction. If the dike is thin compared to its depth, whatever response in ρ_{yx} and ϕ_{yx} is measured, even though it can be modeled with a 2-D TM algorithm, may be very weak. On the other hand, if the strike extent of the dike is large compared to its depth, a strong response in ρ_{xy} and ϕ_{xy} may exist, although this response requires a full 3-D interpretation including the effects of current-gathering. In addition, apart from employing tipper-strike in transverse magnetic mode identification, this 2-D TM approach can make no use of the vertical magnetic field quantities $\tilde{K}_z(\bar{r})$ and $\tilde{Y}_z(\bar{r})$.

As noted in the discussion of regional current-gathering in Figures 15 and 16, the electric field anomaly of our sedimentary basin in the layered host of Figure 12 persists to much greater distances from the body than does the anomaly due to an identical basin in a uniform half-

space. Such effects of the layered host upon electric field anomalies carry over to the apparent resistivity signatures (Ranganayaki and Madden, 1980). In Figure 21, ρ_{xy} and ρ_{yx} have been plotted for a frequency of 0.032 Hz along the y-axis of the 3-D basin model, with both half-space and layered hosts being considered. To the side of the basin within either host, an apparent resistivity anisotropy in excess of an order of magnitude is observed. This anisotropy of course diminishes with distance from the body; with the half-space host, neither ρ_{xy} nor ρ_{yx} depart more than 10% from the 1-D sounding ρ_ℓ beyond distances of about 25 km from the center of the basin. However, the apparent resistivity anomalies about the basin in the layered host exist to considerably greater distances than this. With the layered sequence, ρ_{xy} and ρ_{yx} do not lie within 10% of the ρ_ℓ at this frequency until about 60 km from the center of the basin, which is well off our diagram. We conclude that in the interpretation of MT soundings in the Basin and Range province, not only must one be aware of the sedimentary basin immediately adjacent to the soundings, but perhaps also of basins at greater distances.

We would like to close this subsection on apparent resistivities and impedance phases with a few words on the applicability of one-dimensional inversion in 3-D areas. As explained with Figure 4 and as can be deduced from Figure 13, if the x coordinate axes of all receiver positions are constrained to lie in a uniform direction as we have done, then ρ_{xy} throughout all frequencies experiences a depression relative to the layered host apparent resistivity ρ_ℓ over and to the sides of a conductive 3-D body, but experiences an amplification relative to ρ_ℓ beyond the ends of such a body. On the other hand, as examination of

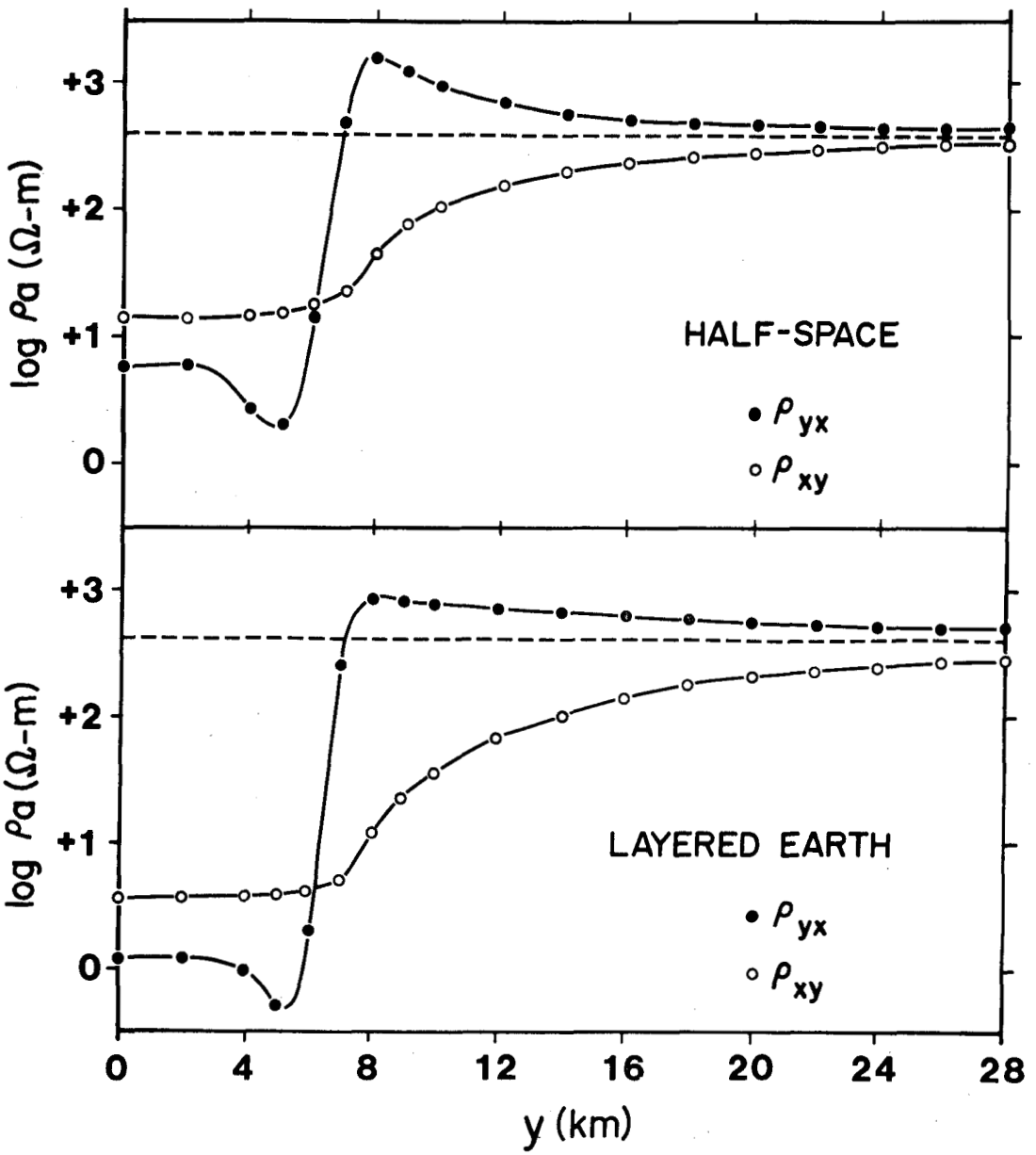

Figure 21. Profiles of apparent resistivities, ρ_{xy} and ρ_{yx} along the y-axis over the 3-D basin model computed for a frequency of 0.032 Hz. The response over the basin in a uniform 400 Ω-m half-space appears in the top half of the diagram for comparison to the response over the basin in the layered host of Figure 12. The 1-D host apparent resistivity ρ_ℓ has also been plotted with dashes for reference for both the half-space and the layered earth.

Figures 4, 5, 13 and 14 will make apparent, if MT strike estimators like those displayed in Figures 17 and 18 are used to define the x coordinate axes of all magnetotelluric functions, i.e, are used to define the TE mode, then ρ_{xy} everywhere over and to the exterior of a conductive 3-D inhomogeneity will be depressed throughout all frequencies relative to ρ_{ℓ} (see also Ting and Hohmann, 1981).

Apparent resistivity and impedance phase soundings identified as transverse electric on the basis of such MT strike estimations are generally employed to obtain models of earth resistivity structure through one-dimensional inversion (Word, et al., 1971; Vozoff, 1972; Stanley et al., 1977; Jiracek et al., 1979; Hermance and Pedersen, 1980; and many others), under the assumption that all near-surface lateral inhomogeneities are essentially two-dimensional as explained following equation (32). In light of the widespread depression with respect to the true layered host sounding ρ_{ℓ} of ρ_{xy}(3-D) defined by MT strike estimators, and given our firm belief that the world is truly three-dimensional, we propose that a great number of layered models of resistivity structure in the literature are, to at least some extent, biased to give erroneously shallow depths to layer interfaces and erroneously low values of layer resistivities (see also Porath, 1971a). This phenomenon may help to explain the dilemma raised by Shankland (1981) and Shankland and Ander (1982) namely, that deep crust and upper mantle temperatures inferred by relating interpreted earth resistivity structure to laboratory rock conductivity measurements are consistently higher than those provided by other methods such as surface heat flow observations or petrological geothermometers, especially in active extensional regimes (Wannamaker et al., 1982).

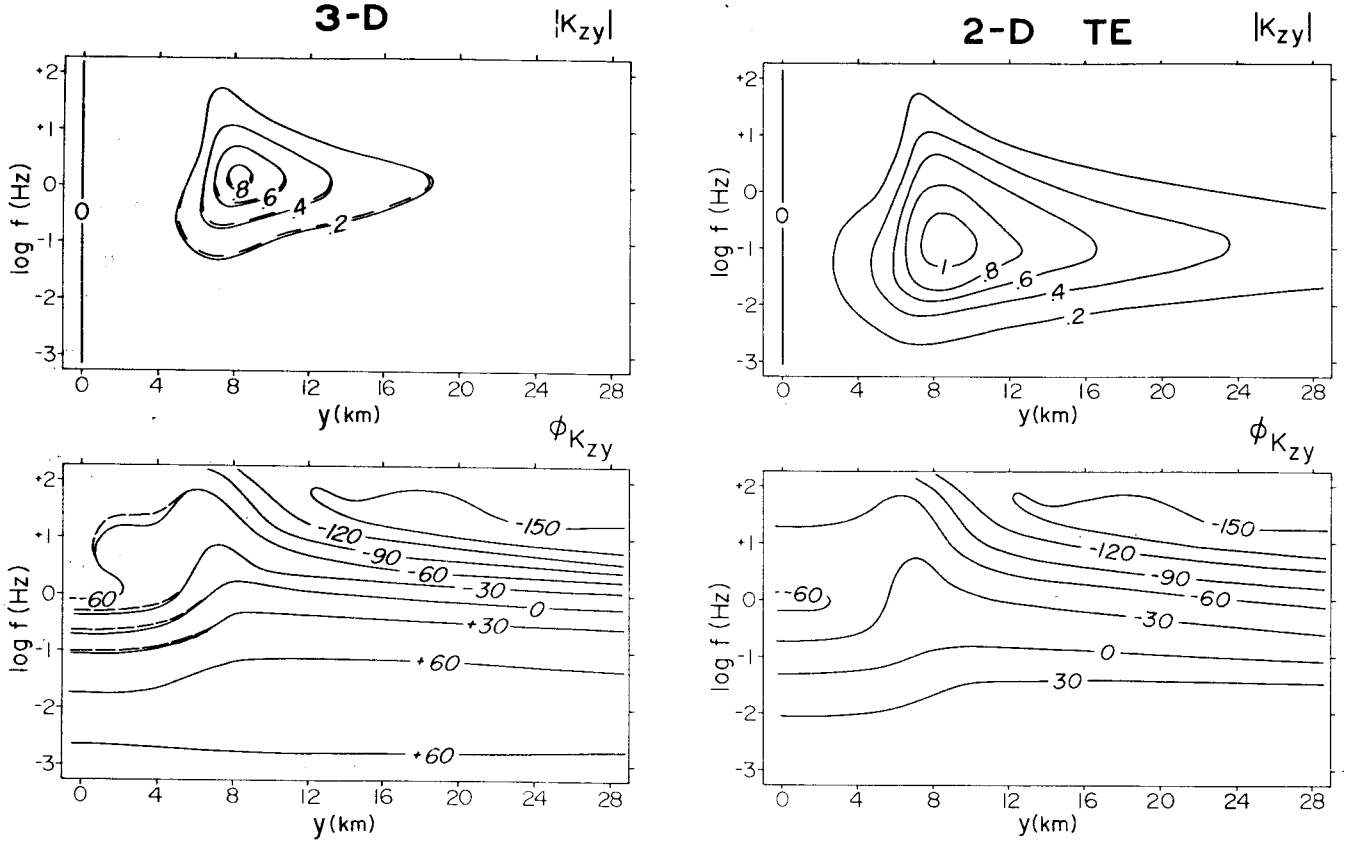

Figure 22. Pseudosections of magnitude and phase of K_{zy} for profiles at x = 0 (solid contours) and x = 9 (dashed contours) over the 3-D basin model compared to 2-D TE pseudosections for corresponding model of infinite strike length. Pseudosections commence at y = 0 over the center of the basin and extend in the y-direction. Contours of magnitude and phase are, respectively, dimensionless and in degrees.

b.) Vertical Magnetic Field Functions. - The strong discrepancy typical between 2-D TE and corresponding 3-D responses is further illustrated by tipper element K_{zy} in Figure 22. The 2-D and 3-D amplitudes agree only above 3. Hz, with the 3-D values at lower frequencies being greatly subdued by comparison. This attenuation of the scattered $\vec{H}$-field in the 3-D case, as explained for ρ_{xy} and ϕ_{xy} previously, results from boundary polarization charges on the ends of the 3-D body. These charges effect a reduction of $\vec{J}_s$ within, and hence $\tilde{Q}_v^o(\bar{r})$ over, the 3-D basin. However, the lack of charges on the 2-D body allows a strong 2-D TE response in $|K_{zy}|$ over a broad frequency range.

Both 2-D and 3-D amplitudes of $|K_{zy}|$ decay rapidly at frequencies below 0.03 Hz in Figure 22. This is caused by the resistivity of the layered host decreasing at depths beyond 15 km, so that $|Z_\ell|$ in equation (40) attenuates quickly at these lower frequencies. Due to this phenomenon, and in light of the strength of the 2-D response, we conclude that large amplitudes of tipper will occur over long, high contrast bodies in hosts that have layer resistivities increasing with depth.

The magnitude of K_{zy} over the 3-D basin model peaks at a frequency near 1. Hz, whereas over our near-surface geological noise model in Figure 7 this quantity peaks at a frequency in excess of 100 Hz. This is an illustration of EM scaling in MT responses, although it is not exact since corresponding dimensions and resistivities of these two models are only approximately similar. The illustration does, however, define the optimum frequencies for calculation of tipper-strike to estimate TE and TM modes of the apparent resistivity and impedance phase

response of our 3-D basin model in the face of small-scale geological noise. For the model structures we have studied, tipper-strike should be computed in the frequency range 0.1 to 1. Hz, to ensure that the basin response in $\tilde{K}_z(\bar{r})$ is strong while that of the geological noise is attenuated (also see Wannamaker et al., 1980).

It is certainly possible that resistivity inhomogeneities of a scale significantly greater than that of typical Basin and Range graben sediments, for instance resulting from regional thermotectonic perturbations common to this province (Eaton, 1982), can dominate tipper amplitudes at frequencies of 0.01 Hz or below (consider Porath, 1971b). This underscores the need for care in defining the term "regional structure" and thus to impose a selective weighting with respect to frequency of one's tipper-strike estimates (cf., Gamble et al., 1982). In light of the strong dependence of tipper responses on both the properties of the body and of the layered host, use of an algorithm like that of Wannamaker and Hohmann (1982) provides the most accurate assessment of this weighting.

Agreement between 2-D and 3-D phases of K_{zy} in Figure 22 is limited to quite high frequencies, above 10 Hz for this model. The inclination of phase contours away from the valley above about 1. Hz is another view of outwardly travelling secondary waves, and corresponds to the rather uniform spacing of contours on single frequency plan maps such as Figure 7. At low frequencies for both 2-D and 3-D valley models, phases of K_{zy} approach the phase of the layered host impedance ϕ_ℓ, which is near 60° at 0.003 Hz.

Over both 2-D and 3-D basin models, $|Y_{zx}|$ approaches a maximum at

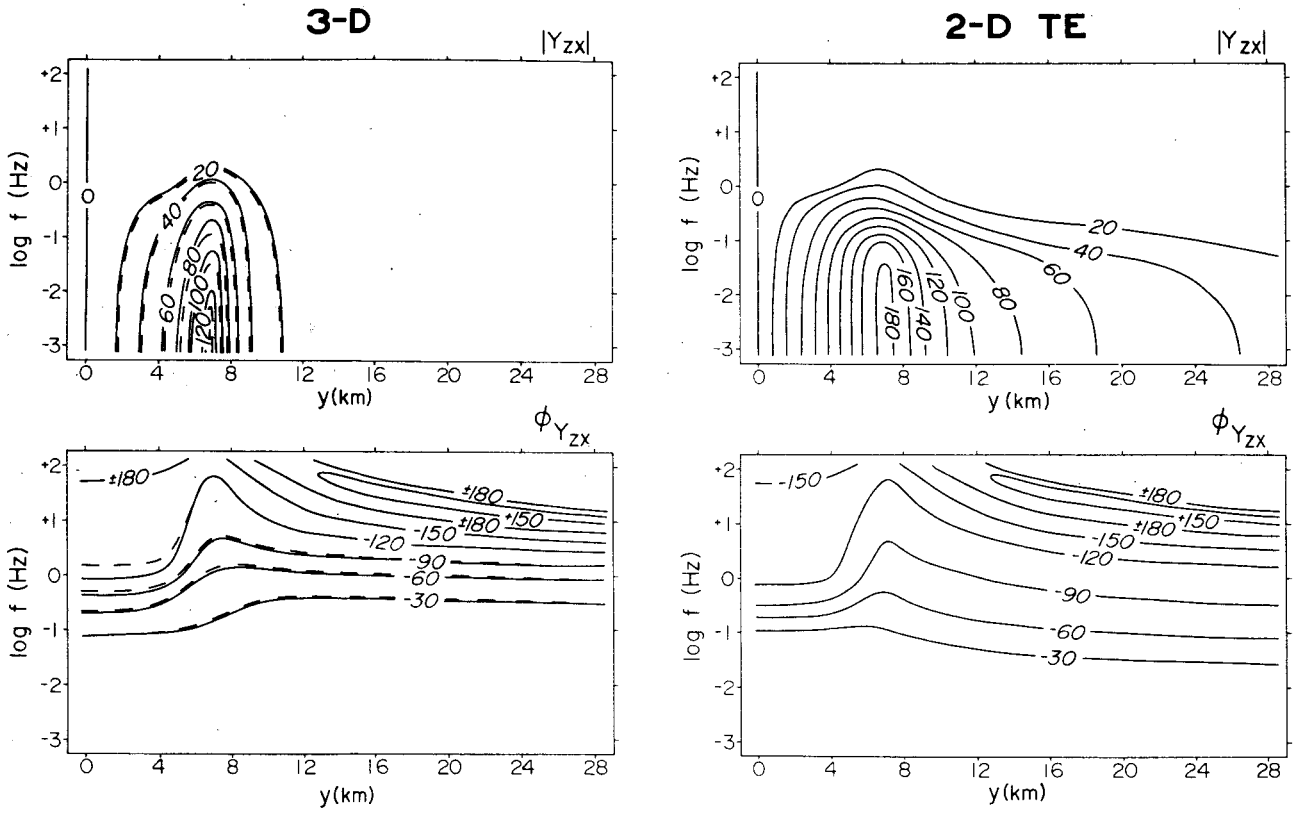

Figure 23. Pseudosections of magnitude and phase of Y_{zx} for profiles at x = 0 (solid contours) and x = 9 (dashed contours) over the 3-D basin model compared to 2-D TE pseudosections for corresponding model of infinite strike length. Pseudosections commence at y = 0 over the center of the basin and extend in the y-direction. Contours of magnitude and phase are in S and degrees.

the very lowest frequencies (Figure 23). This is because the scattered $\vec{H}$-field tensor $\tilde{Q}_v^o(\bar{r})$ in equations (16) and (39) approaches a non-zero low-frequency limit for both 2-D and 3-D models; i.e., a 2-D TE anomaly in $\tilde{Y}_z(\bar{r})$ does not decay to zero at low frequencies as do TE anomalies in apparent resistivity, impedance phase and tipper. We also point out that the amplitude of the anomaly in $\tilde{Y}_z(\bar{r})$ over the 3-D basin model is often greater than 100 S, whereas the amplitude over the small-scale, near-surface structure in Figure 7 seldom exceeds 5 S. This is a manifestation of EM scaling in the MT method, as explained with equation (57), whereby the response in $\tilde{Y}_z(\bar{r})$ due to a large structure exceeds that of a small structure essentially by the geometrical scale factor distinguishing the two structures. Bear in mind, however, that current-gathering in small-scale, 3-D geological noise can distort the response in $\tilde{Y}_z(\bar{r})$ of a large structure such as a sedimentary basin to arbitrarily low frequencies, as explained with equation (72), even though the amplitude of the anomaly in $\tilde{Y}_z(\bar{r})$ due to the geological noise alone may be small compared to the anomaly due just to the large structure.

As was the case for K_{zy}, 2-D and 3-D phases of Y_{zx} in Figure 23 agree closely only for frequencies exceeding 10 Hz, and the phase contours again appear inclined away from the basin. At low frequencies, consistent with equation (41), phases approach zero over both 2-D and 3-D bodies.

Given the size of the basin model, the frequencies at which 2-D TE and corresponding 3-D MT responses agree closely may seem surprisingly high. Wannamaker and Hohmann (1982), however, explain that the length a 3-D body must have to achieve agreement with 2-D TE components depends

strongly on the 1-D host, with bodies in layers overlying resistive basements needing to be much longer than bodies overlying conductive basements. Layered host resistivities in nature increase with depth in the upper 10 or more km (Brace, 1971), exacerbating the difficulties with 2-D TE interpretations.

CONCLUSIONS

The electromagnetic fields scattered by a 3-D inhomogeneity have both volume currents and boundary charges as sources. The latter, which result in current-gathering in conductive structures, dominate the secondary electric field at low frequencies. Particularly sensitive are $\vec{E}$-field magnitudes, remaining distorted even as frequency approaches zero. However, phases of the secondary electric and magnetic fields at low frequencies reduce to that of the incident electric field $\vec{E}_i^o$. Neither amplitude nor phase of the secondary magnetic field contribute materially to the total $\vec{H}$-field below certain frequencies, but the nature of the layered host must be considered to understand just when this occurs.

Tensor apparent resistivities and vertical admittance element magnitudes, since they involve $\vec{E}$-field magnitudes, remain anomalous as frequency falls. Apparent resistivities outside the range of true earth resistivities may exist, in particular very small values occur over shallow conductors. The distortion of apparent resistivities documented in our model studies indicates that one-dimensional inversion of soundings, either near 3-D geological noise or near large-scale sedimentary basins like those in the Basin and Range, offers estimates of host layer resistivities and interface depths that are potentially in serious error. On the other hand, $|K_{zx}|$ and $|K_{zy}|$, as well as all MT function phases, below certain frequencies are minimally affected by a

given inhomogeneity. The tipper elements, both amplitude and phase, exhibit a strong dependence on the layered host while by contrast the vertical admittance elements are far less sensitive to the layering.

Resistivity structure in nature is an ensemble of inhomogeneities of different scales, and the small structures in this collection may have MT responses as strong as those of the large ones. Superimposed upon the apparent resistivities and the magnitudes of vertical admittance elements measured over buried 3-D targets will be the responses of any nearby geological noise to arbitrarily low frequencies. Fortunately, the responses of the small and large bodies have frequency dependencies that are separated as the square of the geometric scale factor distinguishing the different structures, provided corresponding resistivities are similar. Since the magnitudes of the tipper elements as well as the phases of all MT functions due to a particular body are significant only over a finite frequency range, i.e., they are band-limited, then these quantities may allow one to "see through" geological noise to observe the signature of a buried target if the scales of the two types of structure are sufficiently different. Such a separation of responses in frequency is evident for the geological noise and sedimentary basin simulations we have performed, although the picture is complicated a bit by dissimilarities in body geometry and host layering.

Two-dimensional transverse electric modeling algorithms are of limited value for interpreting 3-D measurements. The 2-D TE mode includes no boundary charges, and hence no current-gathering, in its formulation so that the secondary $\vec{E}$-field in this case contributes

negligibly to the MT response as frequency falls. Current-gathering in a 3-D inhomogeneity corresponding to this mode leads to a widespread depression of the total electric field to the side of the 3-D body that is increasingly pronounced toward lower frequencies. Furthermore, while current-gathering can enhance the secondary magnetic field compared to that induced over an equivalent 3-D body in free space, it results in a greatly subdued secondary $\vec{H}$-field compared to that induced by a 2-D structure of identical cross-section. Sedimentary basins constitute very large inhomogeneities, yet only for frequencies above 1. Hz, and sometimes even 10 Hz, do 2-D TE and corresponding 3-D responses for the model we have chosen closely agree.

It is fortunate, therefore, that our model studies have shown that profiles of apparent resistivity ρ_{yx} and impedance phase ϕ_{yx} across elongate 3-D prisms can be modeled accurately with a 2-D TM algorithm. Boundary polarization charges are included in both 3-D and 2-D TM formulations, allowing a proper treatment of current-gathering effects on apparent resistivity and impedance phase. To define pseudosections for transverse magnetic modeling, we recommend employment of a coordinate system based on tipper-strike. Since $\tilde{K}_z(\bar{r})$ is band-limited, one may choose an optimal frequency for defining a tipper-strike to minimize the contributions of secondary structures much smaller or, for that matter, much larger than one's target. We recognize the limitations of this 2-D TM philosophy but, until additional advances in multi-dimensional modeling take place, this approach provides the only rigorous means of interpreting magnetotelluric measurements in three-dimensional environments.

ACKNOWLEDGEMENTS

We thankfully recognize the constructive review of Dr. William R. Sill and the helpful discussions with William R. Petrick, William A. SanFilipo, and John A. Stodt. Also, Terry J. Killpack and Carleen Nutter provided valuable guidance in operation of the Prime 400 computer, upon which the model results were computed. The manuscript was typed by Joan Pingree and Nancy Rivera, while the figures were prepared by Fred Garlock, Brad Wixom, Pat Daubner, Connie Pixton and Doris Cullen.

This research was supported by DOE/DGE contract DE-AC07-80ID12079.

REFERENCES

Berdichevsky, M. N., and Dmitriev, V. I., 1976, Basic principles of interpretation of magnetotelluric curves, In Geoelectric and Geothermal Studies, A. Adam, ed., Akademini Kiado, Budapest.

Boehl, J. E., Bostick, F. X., Jr., and Smith, H. W., 1977, An application of the Hilbert transform to the magnetotelluric method: Elec. Geop. Res. Lab. Rep., Univ. of Texas at Austin, 98 p.

Brace, W. F., 1971, Resistivity of saturated crustal rocks to 40 km based on laboratory measurements, In The Structure and Physical Properties of the Earth's Crust, ed. by J. G. Heacock, American Geophysical Union Mono. 14, p. 243-256.

Cagniard, L., 1953, Basic theory of the magnetotelluric method of geophysical prospecting: Geophysics, 18(3), p. 605-635.

Eaton, G. P., 1982, The Basin and Range province: origin and tectonic significance: Ann. Rev. Earth Plan. Sci., 10, p. 409-440.

Gamble, T. D., Goubau, W. M., and Clarke, J., 1979, Magnetotellurics with a remote reference: Geophysics, 44 (1), p. 53-68.

Gamble, T. D., Goubau, W. M., Miracky, R., and Clarke, J., 1982, Magnetotelluric regional strike: Geophysics, 47(6), p. 932-937.

Grant, F. S., and West, G. F., 1965, Interpretation Theory in Applied Geophysics: McGraw-Hill Book Company, Toronto, 584 p.

Hermance, J. F., and Pedersen, J., 1980, Deep structure of the Rio Grande Rift: a magneotelluric interpretation: J. Geop. Res., 85(B7), p. 3899-3912.

Hintze, L. F., 1980, Geologic map of Utah: Utah Geological and Mineral Survey, Salt Lake City, Utah.

Jiracek, G. R., Ander, M. E., and Holcombe, H. T., 1979, Magnetotelluric soundings of crustal conductive zones in major continental rifts, In Rio Grande Rift: Tectonics and magmatism, ed. by R. E. Reiker, American Geophysical Union, Washington, p. 209-222.

Jones, F. W., and Vozoff, K., 1978, The calculation of magnetotelluric quantities for three-dimensional conductivity inhomogeneities: Geophysics, 43 (6), p. 1167-1175.

Jupp, D. L., and Vozoff, K., 1976, Discussion on "The magnetotelluric method in the exploration of sedimentary basins" by K. Vozoff: Geophysics, 41 (2), p. 325-328.

Klein, D. P., and Larsen, J. C., 1978, Magnetic induction fields (2-30 cpd) on Hawaii Island and their implications regarding electrical conductivity in the oceanic mantle: Geop. J. R. Ast. Soc., 53, p. 61-77.

Kunetz, G., 1972, Processing and interpretation of magnetotelluric soundings: Geophysics, 37(6), p. 1005-1021.

Larsen, J. C., 1975, Low frequency (0.1-6.0 cpd) electromagnetic study of the deep mantle electrical conductivity beneath the Hawaiian Islands: Geop. J. R. Ast. Soc., 43, p. 17-46.

_____, 1977, Removal of local surface conductivity effects from low frequency mantle response curves, Acta Geod. Geop. et Mont. Acad. Sci., 12, p. 183-186.

_____, 1981, A new technique for layered earth magnetotelluric inversion: Geophysics, 46(9), p. 1247-1257.

Parker, R. L., and Whaler, K. A., 1981, Numerical methods for establishing solutions to the inverse problem of electromagnetic induction: J. Geop. Res., 86(B10), p. 9574-9584.

Petrick, W. R., Pelton, W. H., and Ward, S. H., 1977, Ridge regression inversion applied to crustal resistivity sounding data from South Africa: Geophysics, 42 (5), p. 995-1005.

Porath, H., 1971a, A review of the evidence on low-resistivity layers in the earth's crust, In The Structure and Physical Properties of the Earth's Crust, ed. by J. G. Heacock, American Geophysical Union Mono. 14, p. 127-144.

_____, 1971b, Magnetic variation anomalies and seismic low-velocity zone in the western United States: J. Geop. Res., 76(11), p. 2643-2648.

Price, A. T., 1973, The theory of geomagnetic induction: Phys. of the Earth and Plan. Int., 7, p. 227-233.

Ranganayaki, R. P., and Madden, T. R., 1980, Generalized thin sheet analysis in magnetotellurics: an extension of Price's analysis: Geop. J. R. Ast. Soc., 60, p. 445-457.

Rijo, L., 1977, Modeling of electric and electromagnetic data: Ph.D. Thesis, Dept. of Geology and Geophysics, Univ. of Utah.

Rooney, D., and Hutton, V. R. S., 1977, A magnetotelluric and magnetovariational study of the Gregory Rift Valley, Kenya: Geop. J. R. Ast. Soc., 51, p. 91-119.

Shankland, T. J., 1981, Electrical conduction in mantle materials, In Evolution of the earth, ed. by R. T. O'Connell and W. S. Fyfe, AGU Geodynamics Series Vol. 5, Washington, p. 256-263.

Shankland, T. J., and Ander, N. E., 1982, Electrical conductivity, temperatures, and fluids in the lower crust: Los Alamos National Laboratory, unpublished manuscript.

Stanley, W. D., Boehl, J. E., Bostick, F. X., Jr., and Smith, H. W., 1977, Geothermal significance of magnetotelluric soundings in the Snake River Plain -- Yellowstone region: J. Geop. Res., 82 (17), p. 2501-2514.

Stodt, J. A., 1978, Documentation of a finite element program for solution of geophysical problems governed by the inhomogeneous 2-D scalar Helmholtz equation: NSF Program Listing and Documentation, Univ. of Utah, 66 p.

_____, 1982, Bias removal for conventional MT data: ESL Report, in press, Salt Lake City.

Stratton, J. A., 1941, Electromagnetic Theory: McGraw-Hill International Series in Pure and Applied Physics, McGraw-Hill Book Company, New York, 615 p.

Swift, C. M., 1967, A magnetotelluric investigation of an electrical conductivity anomaly in the southwestern United States: Ph.D. thesis, Massachusetts Institute of Technology, 211 p.

Ting, S. C., and Hohmann, G. W., 1981, Integral equation modeling of three-dimensional magnetotelluric response: Geophysics, 46 (2), p. 182-197.

Vozoff, K., 1972, The magnetotelluric method in the exploration of sedimentary basins: Geophysics, 37 (1), p. 98-141.

Wannamaker, P. E., Ward, S. H., Hohmann, G. W., and Sill, W. R., 1980, Magnetotelluric models of the Roosevelt Hot springs thermal area, Utah: ESL Report DOE/ET/27002-8, 213 p.

Wannamaker, P. E., and Hohmann, G. W., 1982, Electromagnetic modeling of three-dimensional bodies in layered earths using integral equations: ESL Report 64, Salt Lake City, 50 p.

Wannamaker, P. E., Ward, S. H., Hohmann, G. W., and Sill, W. R., 1982, Deep resistivity structure in southwestern Utah and its geothermal significance: Univ. Utah, Dept. Geology, DOE/ID/12079-89, 83 p.

Ward, S. H., 1967, Electromagnetic theory for geophysical application: Mining Geophysics, v. II, Tulsa, SEG.

Ward, S. H., Parry, W. T., Nash, W. P., Sill, W. R., Cook, K. L., Smith, R. B., Chapman, D. S., Brown, F. H., Whelan, J. A., and Bowman, J. R., 1978, A summary of the geology, geochemistry and geophysics of the Roosevelt Hot Springs thermal area, Utah: Geophysics, 43 (7), p. 1515-1542.

Weinstock, H., and Overton, W. C., Jr., 1981, SQUID applications in geophysics: SEG, Tulsa, 208 p.

Word, D. R., Smith, H. W., and Bostick, F. X., Jr., 1971, Crustal investigations by the magnetotelluric impedance method, In The Structure and Physical Properties of the Earth's Crust, ed. by J. G. Heacock, American Geophysical Union Mono. 14, p. 145-167.

APPENDIX A

NUMERICAL TEST OF THE COUPLED BODY APPROXIMATION

Since a great number of conclusions in this paper are based upon our coupled body theory, it is of great importance that the accuracy of the approximation be verified. In Figure A-1, a small plate-like conductor, 1800 m by 7 km by 350 m thick with a depth to top of 350 m, lies next to a much larger conductor 15 km by 36 km by $1\frac{1}{2}$ km thick buried $1\frac{1}{2}$ km. The intrinsic resistivity of the smaller feature is 40 Ω-m while that of the bigger is 3 Ω-m. These small and large plates represent structures A and B of the section on coupled body theory.

Initially, $\vec{J}_s$ in the small and big plates coupled together was computed for two polarizations of $\vec{E}_i^o$ at 0.3 Hz. Using the scattering current in just the small body, equations (11) and (12) were evaluated numerically to obtain the secondary fields due only to the small body. These fields we refer to as the "true" secondary fields resulting from structure A. Next, $\vec{J}_s$ within the large and small bodies was calculated separately, again for two polarizations of $\vec{E}_i^o$ at 0.3 Hz. Secondary fields were then calculated over the small body in the absence of the bigger, are named the "unperturbed" fields, and correspond to $\vec{E}_{sA}^o(\bar{r})$, $\vec{H}_{sA}^o(\bar{r})$ and $\vec{H}_{zA}^o(\bar{r})$ in equations (57), (58) and (65). Finally, after the total $\vec{E}$-field over the larger body in the absence of the smaller was calculated, corresponding to $\vec{E}_{tB}^o(\bar{r}_A)$ in (59), relations

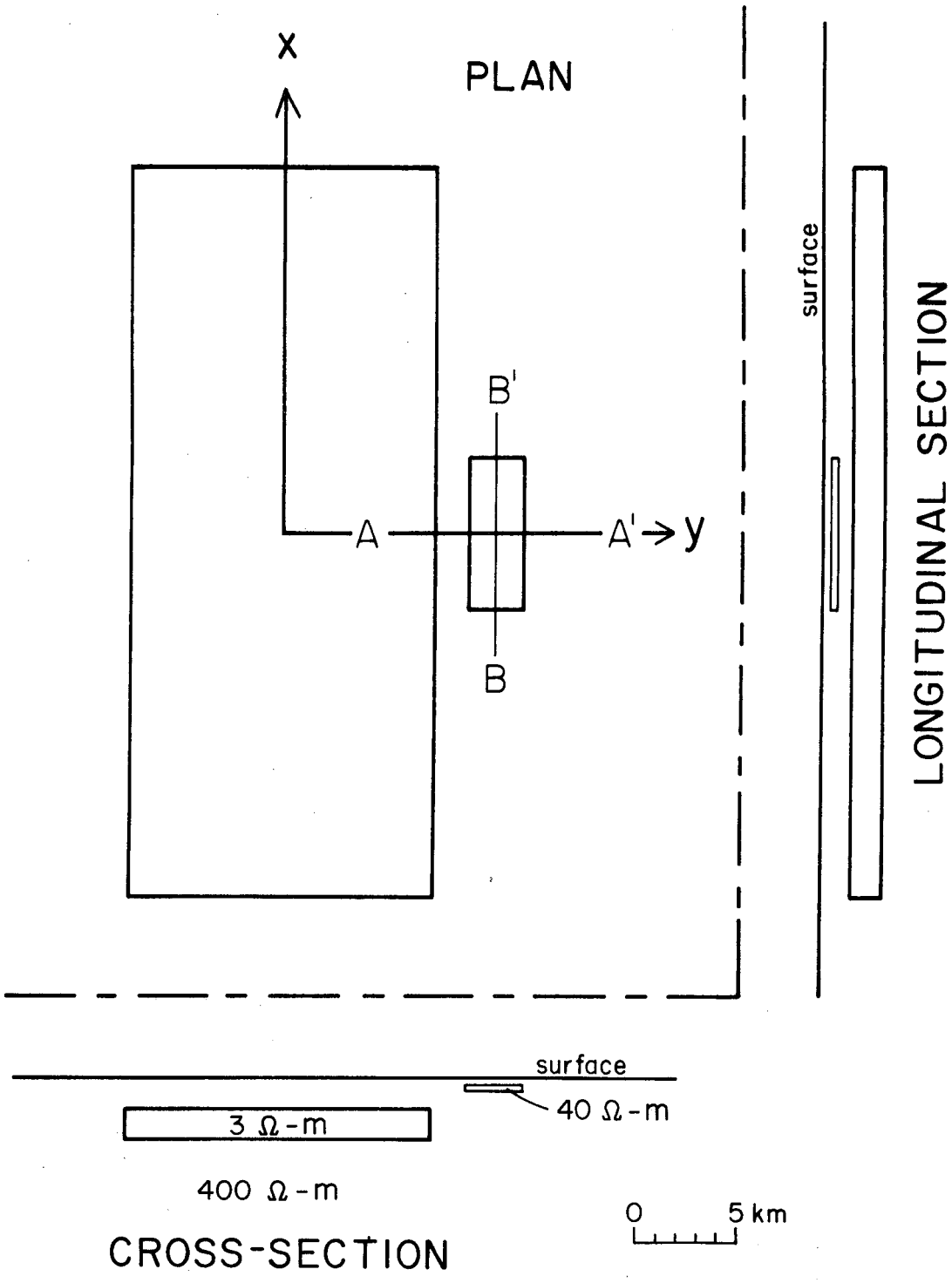

Figure A-1. Multiple inhomogeneity assembly used to test the coupled body approximation. The small and large bodies represent structures A and B of the section on coupled body theory.

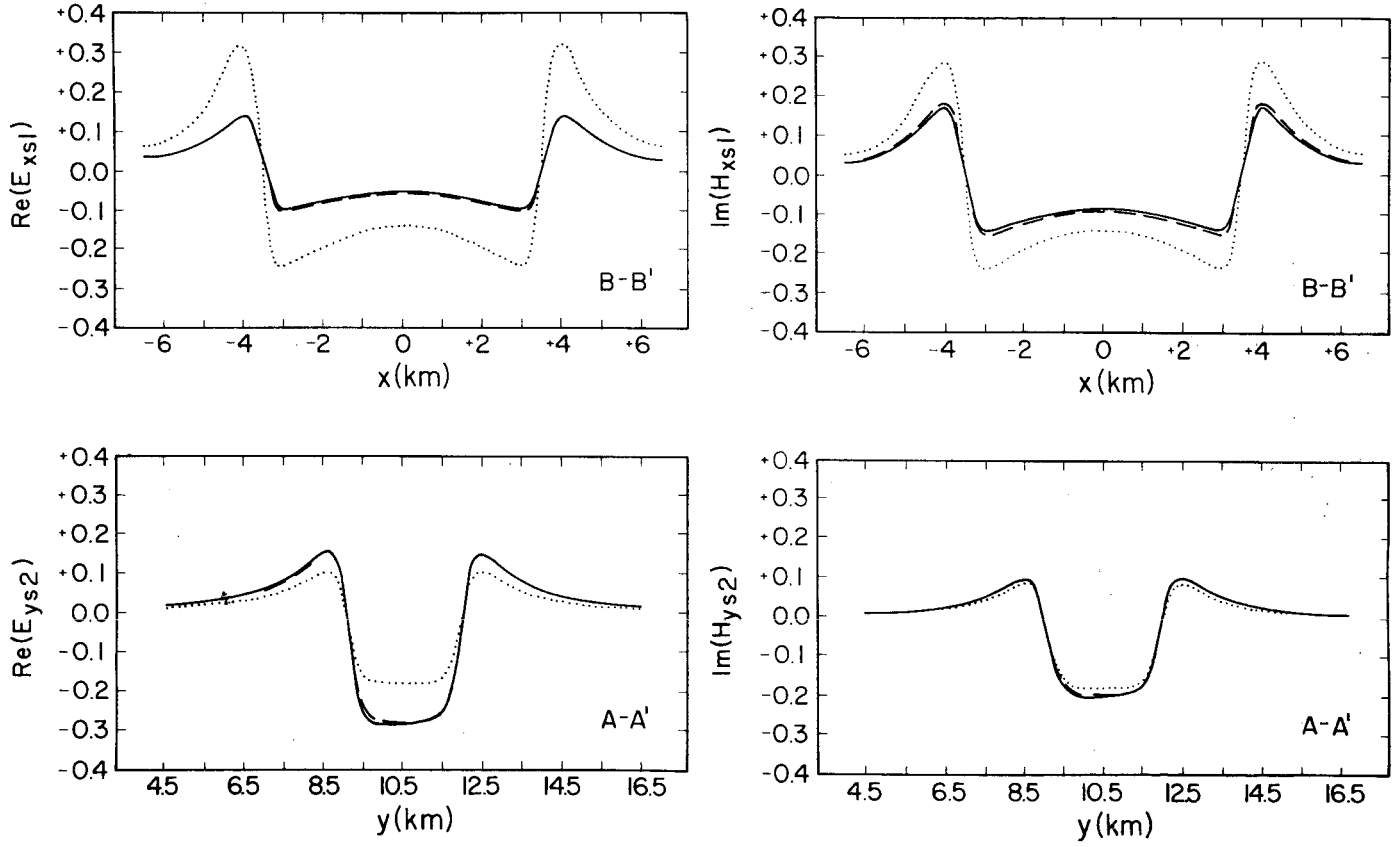

Figure A-2. Plots of true (solid lines), unperturbed (dotted lines) and estimated (dashed lines) secondary electric fields at 0.3 Hz over the smaller body of Figure A-1. The profile along which the fields were calculated is labeled in the lower righthand corner of each graph. The values of the real and imaginary parts have each been normalized by the magnitude of the incident electric field at the surface $\tilde{E}_i^0$.

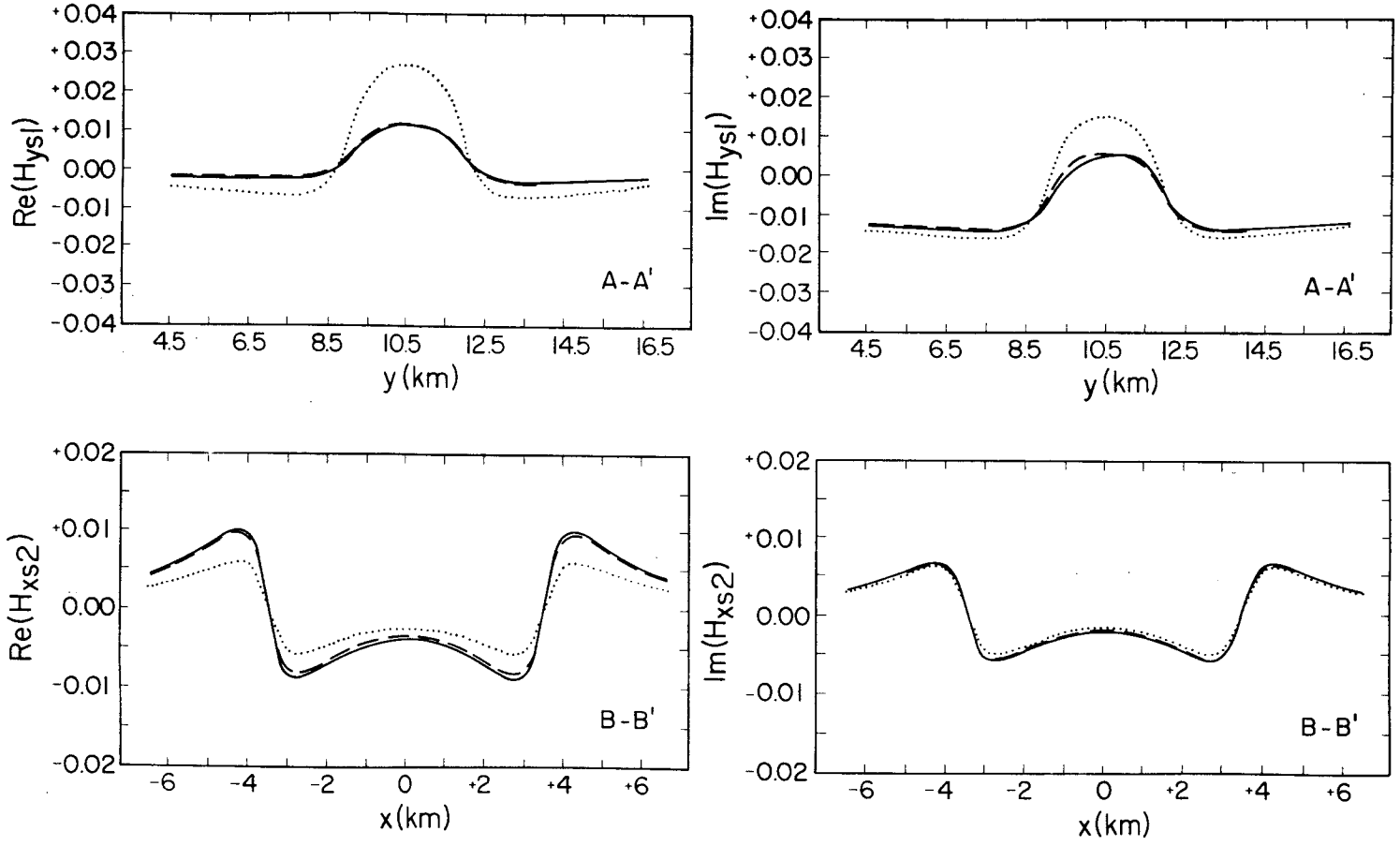

Figure A-3. Plots of true (solid lines), unperturbed (dotted lines) and estimated (dashed lines) secondary horizontal magnetic fields at 0.3 Hz over the smaller body of Figure A-1. The values of the real and imaginary parts have each been normalized by the magnitude of the incident magnetic field at the surface $\vec{H}^0_i$.

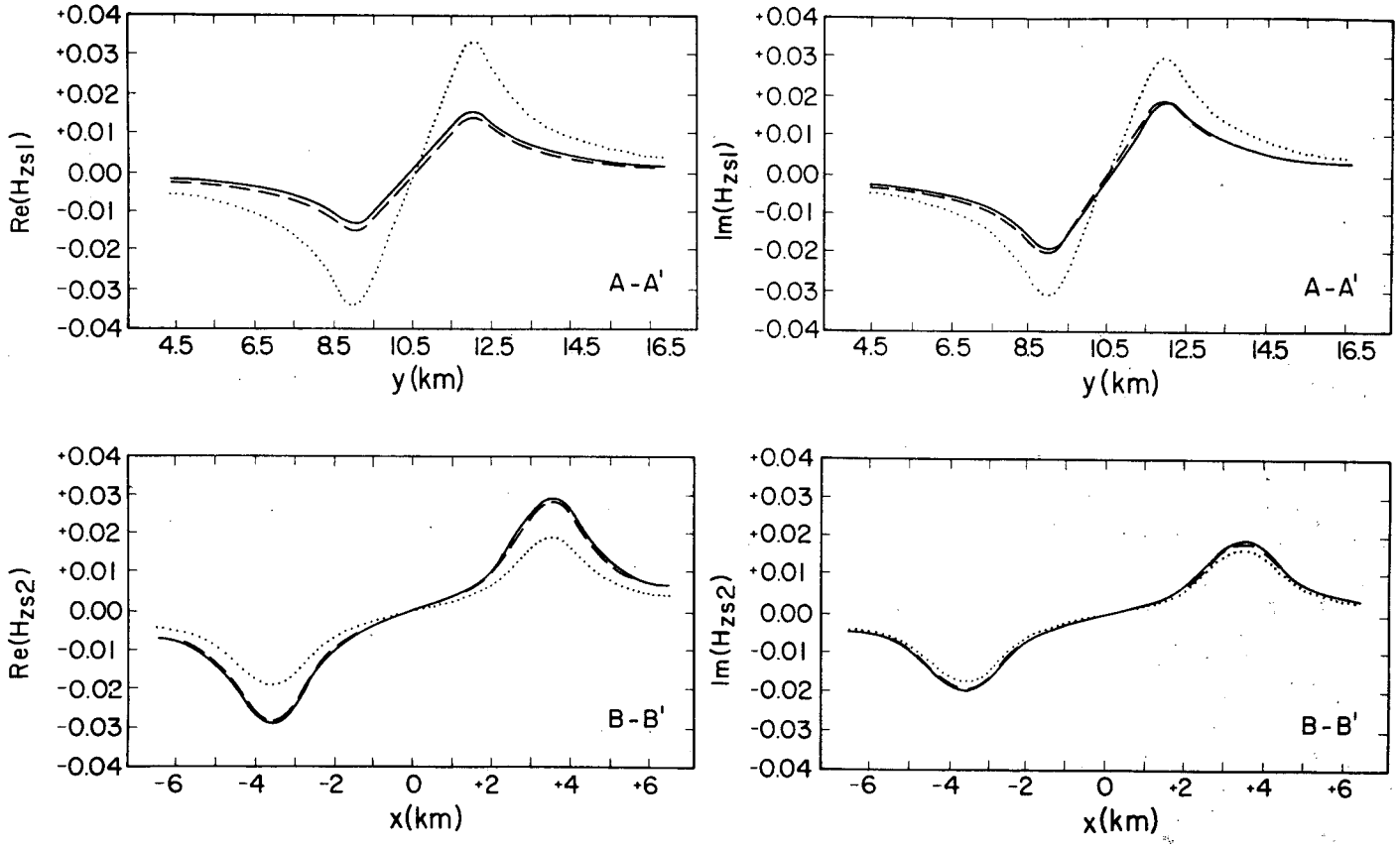

Figure A-4. Plots of true (solid lines), unperturbed (dotted lines) and estimated (dashed lines) secondary vertical magnetic fields at 0.3 Hz over the smaller body of Figure A-1. The values of the real and imaginary parts have each been normalized by the magnitude of the incident magnetic field at the surface $\vec{H}_i^0$.

(61), (62) and (66) yielded $\vec{E}^{o'}_{sA}(\bar{r})$, $\vec{H}^{o'}_{sA}(\bar{r})$ and $\vec{H}^{o'}_{zA}(\bar{r})$. These are referred to subsequently as "estimated" secondary fields.

Plots of true, unperturbed and estimated secondary fields at 0.3 Hz, normalized by the incident $\vec{E}$- and $\vec{H}$-fields on the surface, for the profiles A-A' and B-B' of Figure A-1 appear in Figures A-2, A-3 and A-4. For example, E^{o}_{xs1} stands for a secondary $\vec{E}$-field in the x-direction due to the first polarization of incident field. The first polarization of $\vec{E}^{o}_{i}$ is along the x-axis while the second is along y.

The agreement between true and estimated fields is quite close; nowhere is it worse than 10% and in general it is much better. Slight asymmetries in the true E^{o}_{ys2}, H^{o}_{ys1} and H^{o}_{zs1} are due to slight asymmetries in $\vec{J}_s$ within the small plate, which in turn is due to its proximity to the larger inhomogeneity. Since the coupled body approximation assumes uniform source fields over the small body, the estimated fields must be symmetric across its axes. Both the true and the estimated fields disagree substantially with the unperturbed fields. Hence, a simple addition of the unperturbed fields over the small body alone to the total fields over the large body alone would yield a poor approximation to the true coupled response.